ABSTRACT

Title of Document: EXPERIMENTAL STUDY OF SOLITONS ON INTENSE ELECTRON BEAMS

Yichao Mo, Master of Science, 2012

Directed By: Professor Rami Alfred Kishek
Professor Patrick Gerald O'Shea
Department of Electrical and Computer Engineering

Solitons are localized persistent waves that behave like particles, preserving their properties (shape, velocity, etc.) over long distances and through collisions with other solitons. They have practical applications and are of interest to many disciplines such as condensed matter physics, plasma physics, beam physics, optics, biology and medicine. Whereas solitons in electron beams have been predicted on theoretical grounds decades ago, they have been observed experimentally only recently by Thangaraj at the University of Maryland Electron Ring (UMER). In this thesis, I report on the first systematic characterization of solitons in electron beams and confirm the soliton's particle-like behavior.

The transient longitudinal space charge force on the beam bunch can launch large-amplitude waves, for example from imperfections in matching the focusing force to the beam bunch. By introducing a pulsed laser beam on a thermionic cathode, an electron beam with a narrow density perturbation is generated. The

perturbation then evolves into longitudinal space charge waves that propagate along the beam. For large-amplitude initial perturbations, a soliton wave train is observed. The experimental results are reproduced by simulations with the WARP particle-in-cell (PIC) code.

EXPERIMENTAL STUDY OF SOLITONS ON INTENSE ELECTRON BEAMS

By

Yichao Mo

Thesis submitted to the Faculty of the Graduate School of the
University of Maryland, College Park, in partial fulfillment
of the requirements for the degree of
Master of Science
2012

Advisory Committee:
Professor Rami A. Kishek, Chair
Professor Patrick G. O'Shea
Professor Victor L. Granatstein

Dedication

To my family.

Acknowledgements

I am grateful for my advisors Professor Patrick O'Shea and Rami Kishek for their guidance and financial support of my study. Prof. O'Shea got me into the group and inspired me to work hard in accelerator and beam physics. Prof. Kishek is a great mentor, helped me on almost every aspect of research, from theoretical study, simulation work, to presenting and writing skills, and the direct assistance on the revision of this thesis. I would like to thank the UMER staffs: Dr. Donald Feldman, who involved every step of my experimental setup and operation, along with many helpful discussions; Dr. Irving Haber, for his many instructions on the simulation work; Dr. Brian Beaudoin, who I could always turn to when having problems in the lab and many relative questions; Dr. Timothy Koeth, Dr. Santiago Bernal, Dr. Ralph Fiorito for their discussions and encouragement. I'm also thankful for the UMER students Hao Zhang, Kamal Rezaei, and William Stem for the discussions. In addition, I would like to thank Professor Victor Granatstein for serving in the examination committee.

I thank R. Davidson, E. Startsev, H. Qin and I. Kaganovich from PPPL for helpful discussions. We also thank A. Friedman, D. Grote, and J. L. Vay for their support of WARP. This work is supported by the U.S. Department of Energy Offices of High Energy Physics and Fusion Energy Sciences, and the Dept. of Defense Office of Naval Research and the Joint Technology Office.

Table of Contents

List of Tables

List of Figures

Chapter 1: Introduction

1.1 Motivation

Particle accelerators physics have traditionally focused on the high energy frontier for colliding particles, in facilities such as the Large Hadron Collider (LHC) [1], Tevatron [2], and the Stanford Linear Collider (SLC) [3]. Nowadays, there is a shift to a different type of accelerator where beam quality is important, measured by a high phase space density. Example applications are the 4th-generation light sources [4], free electron lasers [5], spallation neutron sources [6] and so on. Such high-quality beams have low emittance and high current, meaning space charge forces are dominant, especially near the source and low-energy part of the machine. Since the space charge force is generally nonlinear for a non-uniform beam distribution, it is important to understand how much it will contribute to beam quality degradation. Any beam degradation from space charge at low energy will be frozen in as the beam is accelerated to relativistic energies, which may cause emittance growth and reduce application performance. Longitudinal energy or density perturbations at low-energy will propagate as waves along the beam, and the modulations thus generated can lead to beam instabilities and microbunching [7]. Studies of space charge waves [8-9] suggest that small initial perturbations will split into two space charge waves, a slow wave and a fast wave, going opposite directions in the beam frame. When the perturbation is large, it is theoretically predicted that solitary waves, evolving according to the Korteweg-deVries (KdV) equations (see sec. 1.2.2), can be generated on the beam [10-11].

1.2 History and Background

Here, we discuss prior work on space charge waves in beams, and on the broader topic of solitons in science.

1.2.1 Space Charge Waves

The study of space charge waves could be traced back to Simon Ramo and W. C. Hahn in the 1930s [12-13], Birdsall and Whinnery in the 1950s [14].

At the University of Maryland, J. G. Wang and D. X. Wang [8, 15] initiated pioneering studies in which they generated controllable perturbations on an electron beam to induce space charge waves In 1990s. The perturbation was generated by modulating the cathode grid pulse of the thermionic gun. Suk [16] extended those studies to explore the effect of a resistive pipe on the wave propagation. He observed the growth of slow wave and decay of fast wave, consistent with analytical calculations. Inspired by the observation of large-amplitude waves, Suk also performed a theoretical analysis of possible solitary wave formation in electron beams, and designed and experiment to test that, but did not carry it out.

Subsequently, at the University of Maryland Electron Ring (UMER), Huo [17] demonstrated a new way of generating perturbations by combining thermionic and photoemission. The long-pulse (~100ns) main beam is produced by thermionic emission, while a short-pulse (~5ns) ultraviolet laser aimed at the cathode produces an additional population of electrons that forms the perturbation. Harris and Neumann [18] extended the work to multiple perturbations using a beam splitter and an interferometer on the drive laser. Thangaraj [19] continued this work, studying the evolution of one or two perturbations over multiple turns around the ring, a distance of over 100 m. Towards the

end of his Ph.D. research, Thangaraj experimented with large-amplitude perturbations and was the first to observe solitary waves on electron beams.

1.2.2 Solitons

Solitons are localized persistent waves that behave like particles, preserving their properties (shape, velocity, etc.) over long distances and through interactions and collisions with other solitons. First observed in water waves by John Scott Russell in Scotland in 1834 [20], the unchanged propagating wave was named "solitary wave", and was later described by the Korteweg and deVries equation in 1898. In 1965, Zabusky and Kruskal solved the KdV equation numerically and observed that the solitary waves behave like stable particles [21], naming it "soliton" afterwards. In 1970, Ikezi, Taylor and Baker observed ion-acoustic solitons in plasma experimentally [22]. Since 1980s, solitons in electron coasting beams were predicted by Bisognano [10] and Davidson [11]. Schamel [23] did theoretical work on solitons in proton beams. In the early 2000s, soliton-like longitudinal oscillations were observed from a stable hump on proton coasting beams [24-25]. More recently, at the University of Maryland Electron Ring (UMER), Thangaraj [19] observed the development of a solitary wave train from large-amplitude perturbations in electron beams.

1.3 Focus of Thesis

In this thesis, we systematically study solitary waves and soliton formation and evolution in intense electron beams. We take advantage of UMER's long propagation distance, and the capability to generate pure density perturbations using the laser photoemission technique first developed by Huo [17]. Since the pioneering work by

Thangaraj, several improvements have taken place, including a reduction in the amount of beam loss over multiple turns, providing more reliable data. Whereas Thangaraj focused on a proof-of-principle experiment for soliton formation, I studied soliton evolution as a function of beam and perturbation parameters, such as beam current. I am also the first to perform two-soliton interaction experiment, demonstrating their particle-like behavior. Finally, I compare the experimental results to self-consistent particle-in-cell simulations, using the simulation to understand more about the experiment.

1.4 Relevant Theory

The classical method for studying space charge waves in electron beams is to apply the one-dimensional cold fluid model [26], where a zero longitudinal temperature and small-amplitude initial perturbation are assumed. By solving the continuity and momentum equations, we get two waves, in the beam frame, propagating in opposite directions with the same phase velocity (or sound speed):

$$C_s = \sqrt{\frac{qg\lambda_0}{4\pi\varepsilon_0\gamma_0^5 m}} \tag{1.1}$$

In Eqn. (1.1), q and m are the charge and mass of beam particles, λ_0 is the unperturbed beam line charge density, γ_0 is the Lorentz factor, ε_0 is the permittivity, and g is the geometry factor [30]:

$$g = \alpha + 2\ln(\frac{b}{a}) \tag{1.2}$$

where a is the beam radius, and b is the pipe radius. α is a constant from 0 to 1. For space-charge-dominated beams, α=0.

When the perturbation amplitude is large, nonlinear effects cannot be ignored. The cold fluid model leads to the Korteweg-deVries (KdV) equation [11, 27]:

$$\frac{\partial u}{\partial t} + u \cdot \frac{\partial u}{\partial z} + \frac{\partial^3 u}{\partial z^3} = 0 . \qquad (1.3)$$

where $u(z,t)$ is the density or velocity perturbation amplitude, as a function of longitudinal distance z and propagation time t. The second term $u \cdot \frac{\partial u}{\partial z}$ represents the nonlinear effect that steepens the perturbation and results in several sub-pulses, while $\frac{\partial^3 u}{\partial z^3}$ is the dispersion term that tends to widen the pulse. The soliton results from the cancellation of these two terms. An analytical one-soliton solution is:

$$u(z,t) = \frac{c}{2} sech^2[\frac{1}{2}\sqrt{c}(z - ct)] . \qquad (1.4)$$

The evolution of a known initial perturbation profile $u(z, t = 0)$ can be found by integrating the KdV equation over a time period τ to obtain $u(z, t = \tau)$. A numerical example is shown in Fig. [1.1], where a soliton train forms from a single initial pulse. We expect a similar perturbation evolution in experiments.

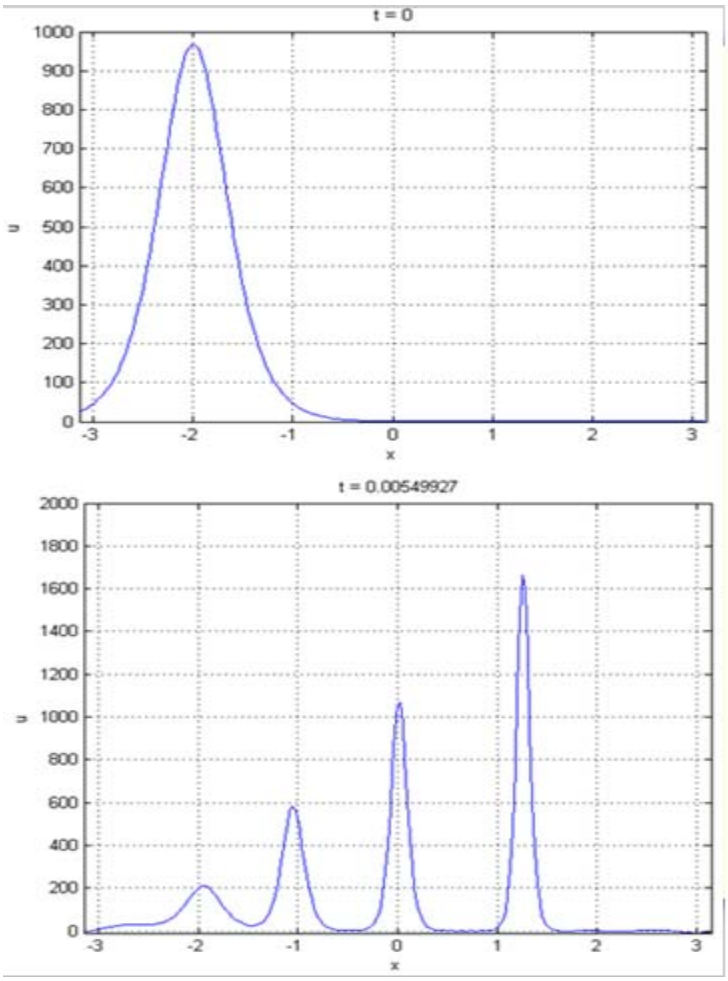

Fig. 1.1: KdV Integration of an initial profile $u(x, t = 0)$ (top) from t=0 to τ =0.00549927 leads to the perturbation profile $u(x, t = \tau)$ (bottom)

1.5 Organization of Thesis

The remainder of the the thesis is organized as follows. In Chapter 2, we introduce the experimental setup, including the UMER gun, the drive laser and perturbation generation, and the diagnostics used. In Chapter 3, we present the detailed experimental results and analysis, along with the simulation study and its comparison with experiments. In Chapter 4, we conclude the work in the thesis and suggest future work that can help better understand solitons in electron beams.

Chapter 2: Experimental Setup

This chapter reviews the experimental setup of the perturbation experiments. First (Sec. 2.1), we briefly introduce the machine used, the University of Maryland Electron Ring (UMER), a storage ring for research on space-charge-dominated beam. Next (Sec. 2.2), we discuss the UMER electron gun, which we use to generate beams from both thermionic emission and photoemission, the photoemission being used to produce perturbations of varying strength and width. Section 2.3 discusses the setup of the photoemission drive laser. Sec. 2.4 reviews the beam diagnostics used in this experiment, mainly the Bergoz coil and wall current monitor. Finally, Sec. 2.5 summarizes the chapter.

2.1 The University of Maryland Electron Ring (UMER)

UMER [Fig. 2.1] is a scaled world-class facility designed for exploring the physics of space charge over a wide range of intensities. It is a circular machine with a circumference of 11.52m. The 10 keV electron beam is injected as a single long bunch, with a duration that we can vary from 25 to 140 ns. By means of apertures [Fig. 2.2] downstream from the anode, we can vary the peak beam current and rms emittance over the range 0.5-100 mA and 0.3-3 μm (normalized), respectively. The basic beam parameters of UMER and apeture are shown in Table 2.1 and 2.2.

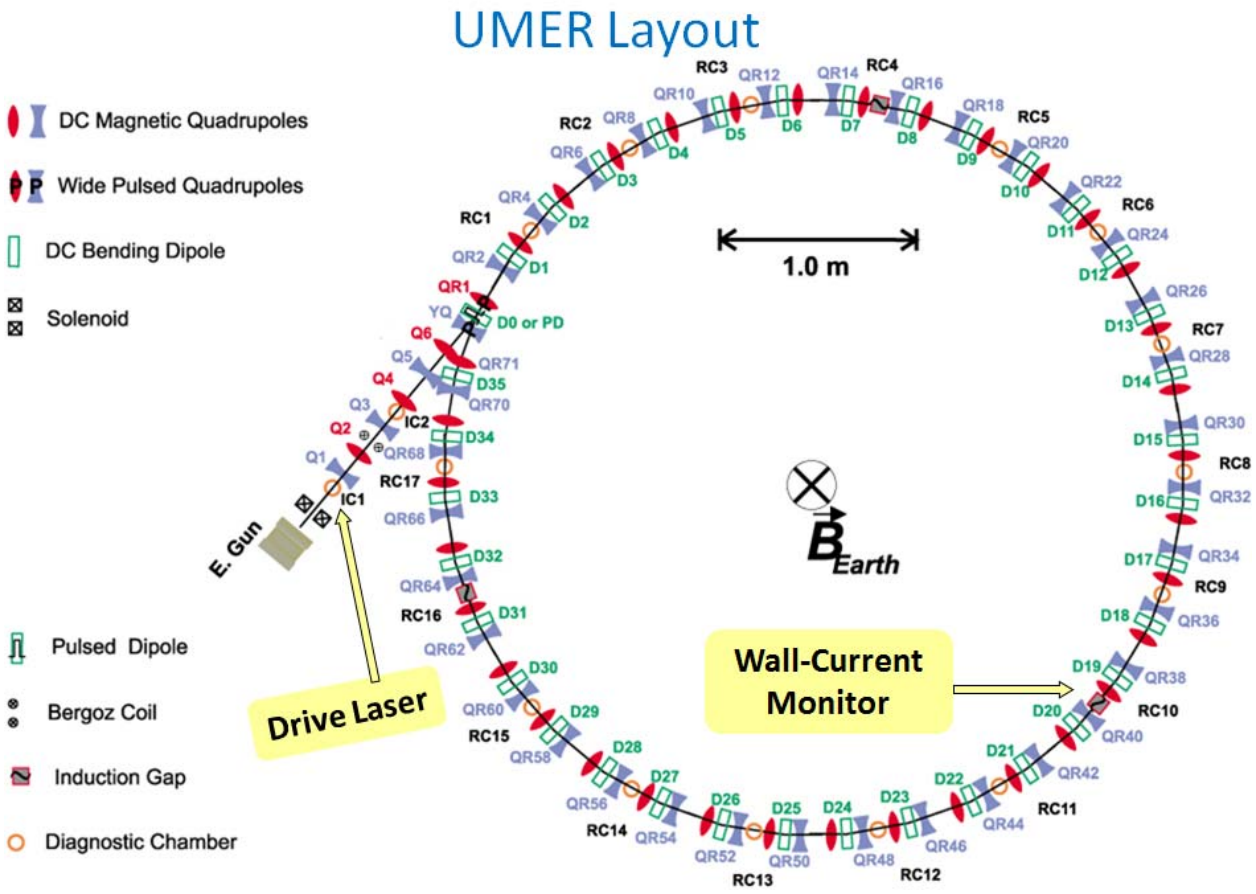

Fig. 2.1: Schematic illustrating the UMER layout (Top view). The arrows indicate the diagnostics used for the experiments described here.

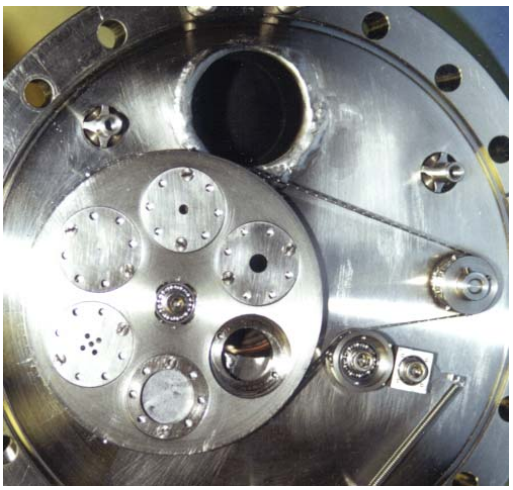

Fig. 2.2: Photograph of the aperture wheel for beam selection, downstream from the anode.

Table 2.1: Beam Parameters of UMER

Beam Energy	10 keV
Beam Velocity (β=v/c)	0.2
Beam Current	0.5-100 mA
Bunch Length (thermionic emission)	25 to 140 ns
Bunch Repetition Rate	10-60 Hz
Circulation Time	197 ns
Circumference	11.52 m
FODO Period	0.32 m
Zero-current Phase Advance	67°

Table 2.2 Aperture Radius and Exiting Beam Current, Emittance

Aperture Raius (mm)	Beam Current (mA)	Normalized Emittance (μm)
0.25	0.6	0.4
0.875	6	1.3
1.5	21	1.5
2.85	78	2.9
Full Beam	104	3.2

UMER consists of a 36-period FODO lattice in the ring, and an injection section with 6 quadrupoles and a solenoid for matching. One of the FODO sections in the ring uses a fast pulsed dipole for injection, after which the polarity of that dipole switches for recirculation. The beam current is measured initially using a Bergoz current transformer located 64 cm downstream from the gun aperture wheel. Details of the transverse distribution are measured in the nearby Diagnostic chamber IC1, as well as at other chambers downstream. IC1 also houses a mirror we use to aim the drive laser onto the

cathode. We use a wall-current monitor at RC10, 7.67 m downstream from the Bergoz, to measure the beam current profile at each turn.

2.2 Electron Gun (Thermionic Emission)

The UMER gun is a gridded Pierce-type gun that has a thermionic dispenser cathode [Fig. 2.3], made of a porous tungsten (W), coated with barium oxide and calcium aluminate. The entire cathode/grid assembly as biased to -10 kV relative to the anode using a dc high-voltage power supply. Under normal operation, a negative bias (15 V) on the cathode grid suppresses electron emission. A larger negative, rectangular, pulse (~36 V), applied on the cathode at a rep rate from 10-60 Hz, is used to extract the electron beam. A Pierce electrode (conical electrode surrounding the cathode with a cone angle of 67.7°) is applied to balance the transverse space charge force to make a uniform laminar beam. The A/K gap can be changed to vary the gun's perveance. For an A/K gap of 25 mm, the gun produces a space-charge limited current of 100 mA, which we can reduce using apertures downstream. For more description about the gun, refer to [28].

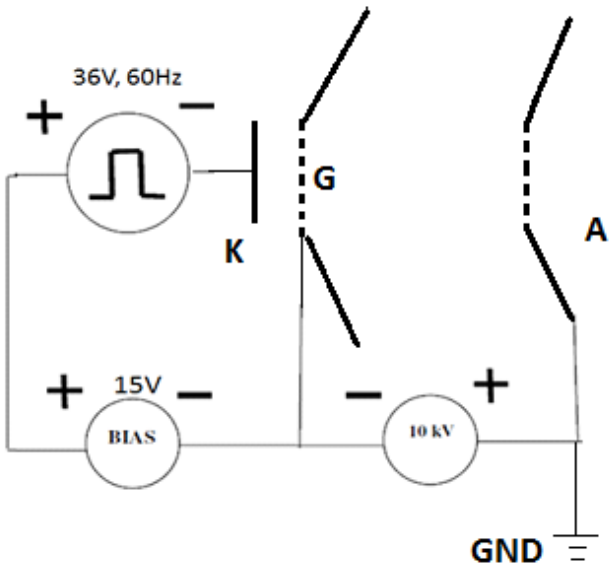

Fig. 2.3: Simplified schematic of UMER gun for thermionic emission.

The gun operates in two modes: temperature-limited mode (650-850 ℃) and space-charge limited mode (>1000 ℃). In the space-charge limited mode, which is used for normal operation, the current is limited by Child-Langmuir law and increasing the heater voltage doesn't affect the current output. For this experiment, I instead operate in the temperature-limited mode so that the photo-emitted electrons generated by the drive laser lead to a perturbation in the beam density. Operating in the temperature-limited mode further allows us to easily adjust the peak beam current by simply changing the cathode temperature. As shown in Fig. 2.4, there is an exponential current growth in the temperature-limited mode (heater voltage between 40V to 50V). Since the temperature-limited does not have saturation, the gun as a triode to amplify any fluctuations in electron density at the cathode. Hence, the beam pulse tends to be noisier than one finds in normal, space-charge-limited operation.

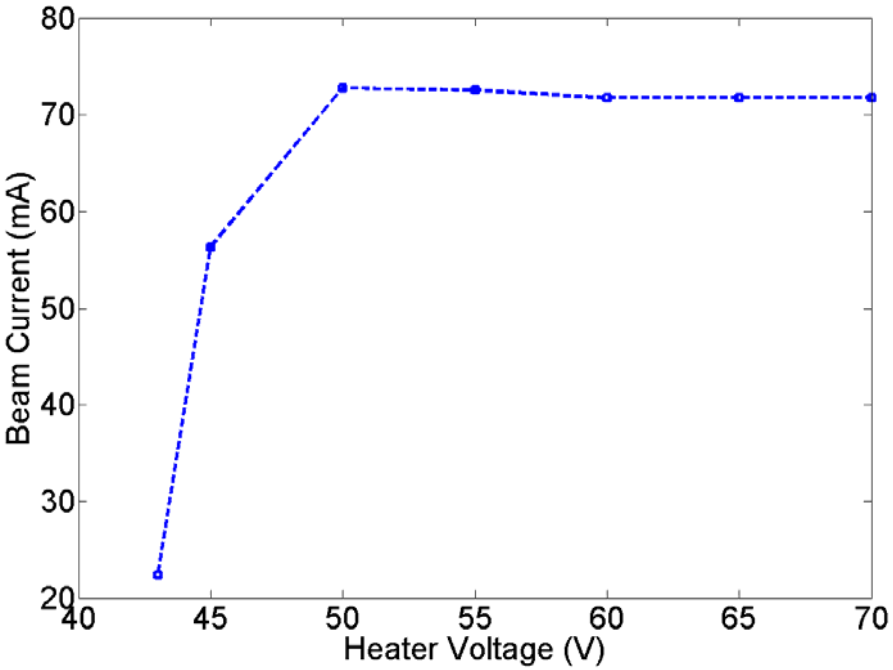

Fig. 2.4: Measured beam current vs heater voltage for the UMER gun (80mA aperture). After an exponential growth, the beam saturates.

To be exact, in our experiment, we are using the 80mA beam aperture, and cool down the cathode (about 40-50V of heater voltage) to produce a beam with peak current in the range 20-40mA. The repetition rate is set to 15Hz to synchronize with the laser for photoemission (see next section).

2.3 Laser Setup (Photoemission)

The UMER gun is also able to generate beams by photoemission [17], which can be applied to introduce a perturbation on the beam. We use a 1064 nm-wavelength Nd-YAG drive laser and triple its frequency with two nonlinear crystals to a wavelength of 355 nm [Fig. 2.5], making the photon energy sufficient to generate photoemission from the cathode. The laser is injected into the chamber (IC1), where it will be reflected by a mirror towards the photocathode. The beam perturbation measured at Bergoz is usually 5-8 ns wide.

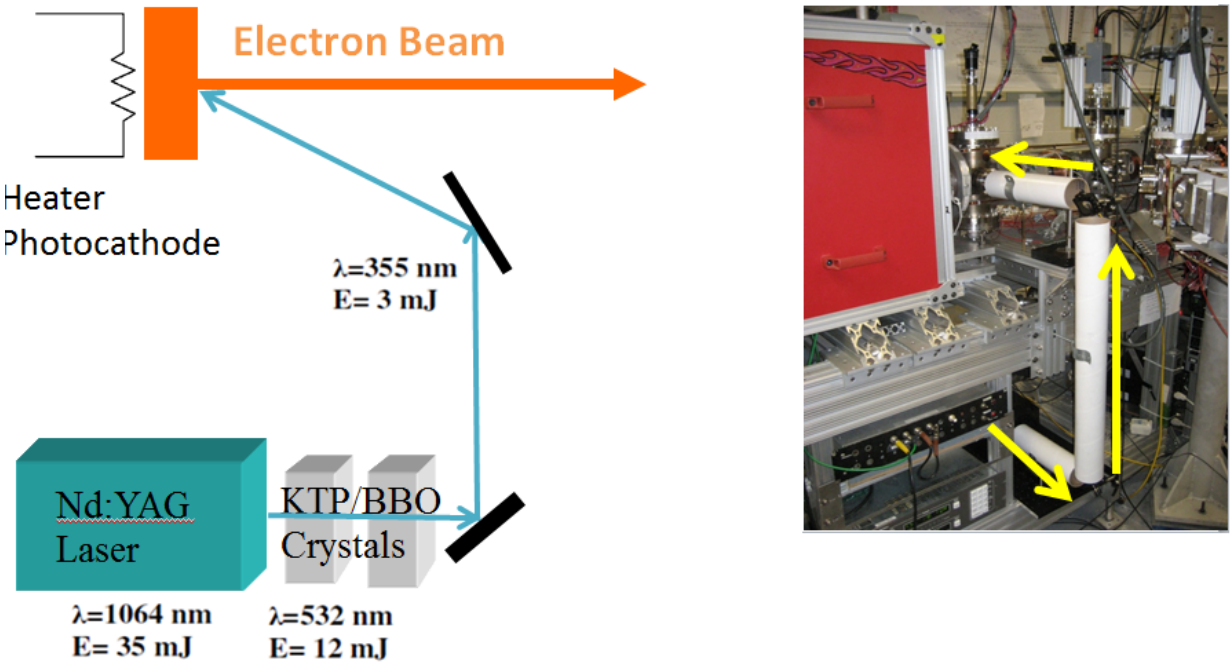

Fig. 2.5: Experimental setup of beam perturbation by photoemission.

The Nd-YAG laser we use is a minilite II model [29]. Table 2.3 lists the basic parameters of this laser. The 3rd harmonic temporal profile is measured by a PIN diode, which is similar to a Gaussian distribution, as shown in Fig. 2.6. The laser alignment is an involved but important process (see Appendix A), which ensures that the laser hits right at the cathode. Due to the synchronization between the triggering source of the beam bunch and pulsed laser, the perturbation is introduced on every beam bunch. By changing the time delay of the laser Q-switch trigger, we can set the perturbation at different locations atop of the beam.

Table 2.3: Nd:YAG Laser Parameters

Wavelength	1064 nm	532 nm	355 nm	266nm
Energy	50 mJ	25 mJ	8 mJ	4 mJ
Peak Power	8.3 MW	6.3 MW	2.0 MW	1.0 MW
Average Power	750 mW	375 mW	120 mW	60 mW
Pulse width	5-7 ns	3-5 ns	3-5 ns	3-5 ns
Stability	2%	3%	4%	8%
Polarization	Horz.	Vert.	Horz.	Horz.
Jitter	< +/- 0.5 ns			
Beam Size	< 3 mm			
Divergence	< 3 mrad			
Repetition Rate	1-15 Hz			

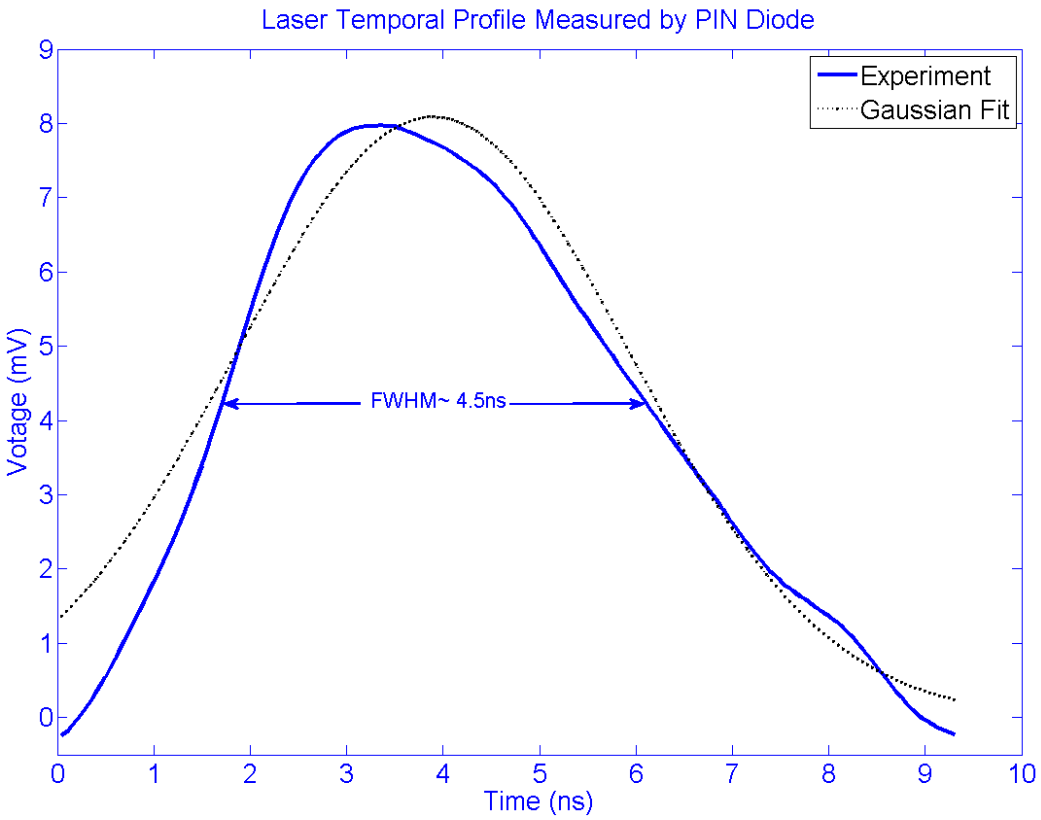

Fig. 2.6: Temporal profile of the 355nm laser for photoemission.

2.4 Beam Diagnostics

As mentioned earlier, the two major diagnostics we use are the Bergoz coil and wall current monitor. **The Bergoz coil** is a fast current transformer, model # FCT-082-20:1, with a rise time down to 200 ps, enabling fast and accurate measurements of the temporal beam current profile. Basically it is a transformer with the beam as the primary. After calibration, the initial beam current is: $I(mA) = 0.8 * U(mV)$, where $U(mV)$ is the output of the transformer.

The Wall current monitor (WCM) is an in-house device we use to give us accurate measurements of the temporal beam current profiles in the ring. It measures

the voltage drop $U(mV)$ across the resistors cause by the image current excited by the beam. The beam current is: $I(mA) = U(mV) / 4.545$ for the UMER calibration.

In addition, we also have **beam position monitor (BPM)** for beam centroid position diagnostics, and **(fast) phosphor screen** for beam imaging diagnostics, to measure the transverse profile and initial emittance [30]. For more details about the above diagnostic tools, refer to [31].

See Fig 2.7 for the difference the laser makes.

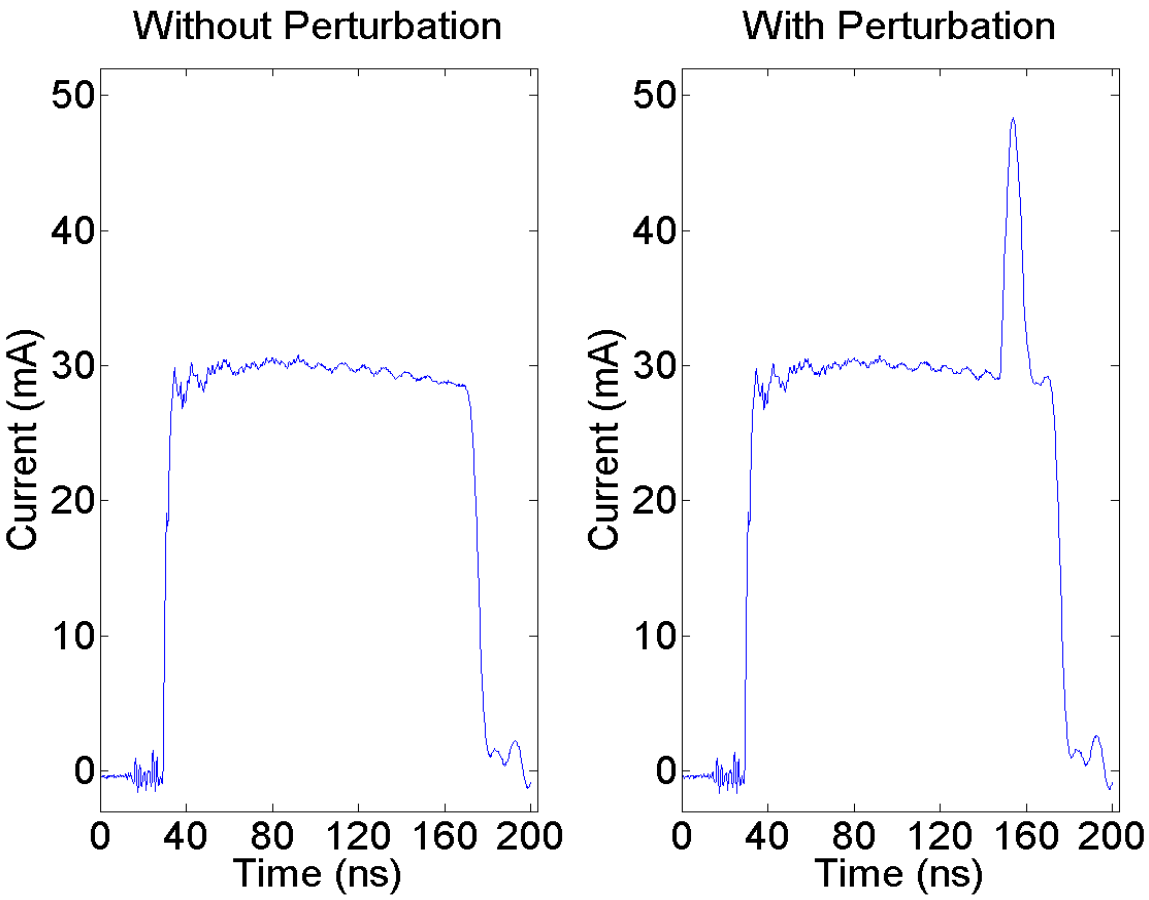

Fig. 2.7: An example output from the Bergoz coil for a beam with and without the perturbation.

2.5 Summary

We discussed the University of Maryland Electron Ring, the two mechanisms of generating electron beams from the gun and how the perturbation experiment is set up. The beam diagnostics methods are shown at last.

Chapter 3: Experimental and Simulation Results

In this chapter, we show our experimental observation of solitons on electron beams and compare the results to simulations. We start (Sec. 3.1) with a representative soliton wave train formed from an initial large-amplitude perturbation. In Sec. 3.2, we discuss the properties of the waves thus formed and demonstrate they are solitons. In Sec. 3.3, we show the soliton dependence on beam parameters like beam current, perturbation strength and width. In Sect. 3.4, we study the soliton interaction by initiating two solitons from two initial large-amplitude perturbations. In Sec. 3.5, we discuss the results of simulations with the WARP code [Appendix B] and compare them with experiments. Section 3.6 addresses some the discrepancies between simulation and experiment. Finally, Sec. 3.7 summarizes the chapter.

3.1 Single Large-Amplitude Initial Perturbation

From previous studies on the space-charge waves, both theoretical using the one-dimensional cold-fluid model and experimental, a small-amplitude initial perturbation launches into two space charge waves, a slow wave and a fast wave. In beam frame, the two waves propagate with same phase velocity (or sound speed, Eqn. 1.1) but towards opposite directions. However, when the perturbation amplitude is large (say >20%), the linear approximation for sound speed derivation no longer stands, and the phase velocity increases with the perturbation strength [31]. Therefore, particles on the crest travels faster than the ones on the trough, and the wave will eventually steepen and develop into multiple sub-pulses. Meanwhile, when the pulse width is comparable to the pipe radius,

the wave becomes dispersive [10] and it can balance the steepening effect, to maintain the pulse shape and lead to solitary wave formation.

Figs. 3.1 and 3.2 are typical experimental results of a nonlinear density perturbation on the beam. In Fig. 3.1, the initial peak current measured at the Bergoz is 22 mA with an additional 11 mA perturbation (we will hence call it a 50% perturbation). The perturbation is introduced near the beam tail to allow the fast wave to propagate longer on the flat-top portion of the beam. Fig. 3.2 depicts the turn-by-turn beam current measured at RC10. The beam current in each turn is plotted on the same scale (centered on the beam pulse), with each turn shifted upward by 20 mA for clarity. For a different way of visualization, Fig. 3.3 is a 3D depiction of the same data in Fig. 3.2. The slow wave steps off the beam edge after the perturbation splits (in Turn 1). Meanwhile, the fast wave moves towards the beam head (to the left in Fig. 3.2), steepens, and develops into several sub-pulses. Starting from about the 4th turn, the sub-pulses maintain their shape in the beam frame (see Sec. 3.2), which is a basic property of solitons. Also, the sub-pulse width is measured to be ~1ns, which is 6 cm long, comparable to the pipe diameter of 5.08 cm.

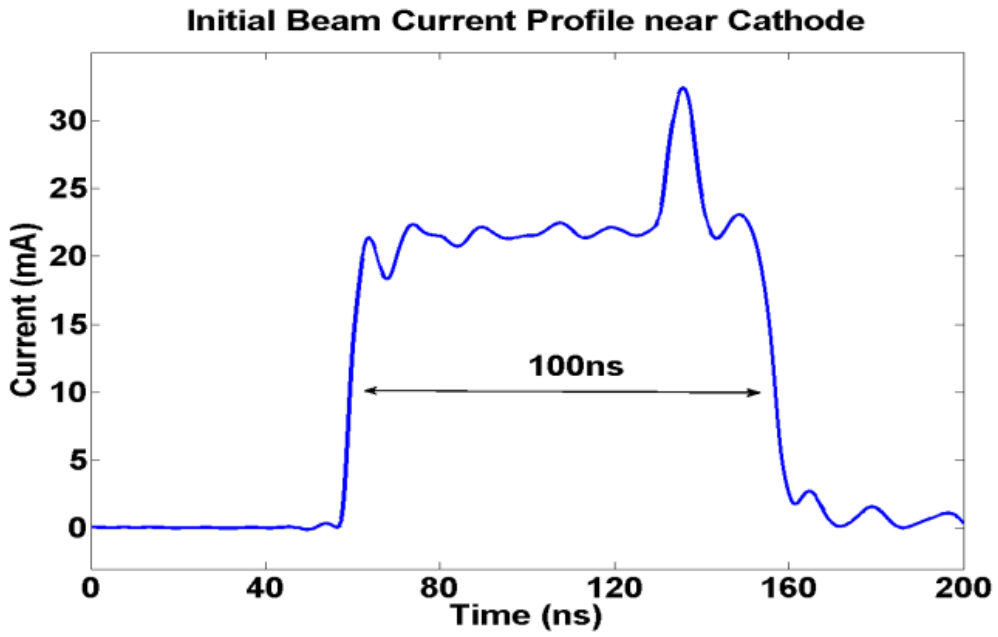

Figure 3.1: Initial beam condition measured at the Bergoz coil, for a 22 mA beam and a 50% perturbation.

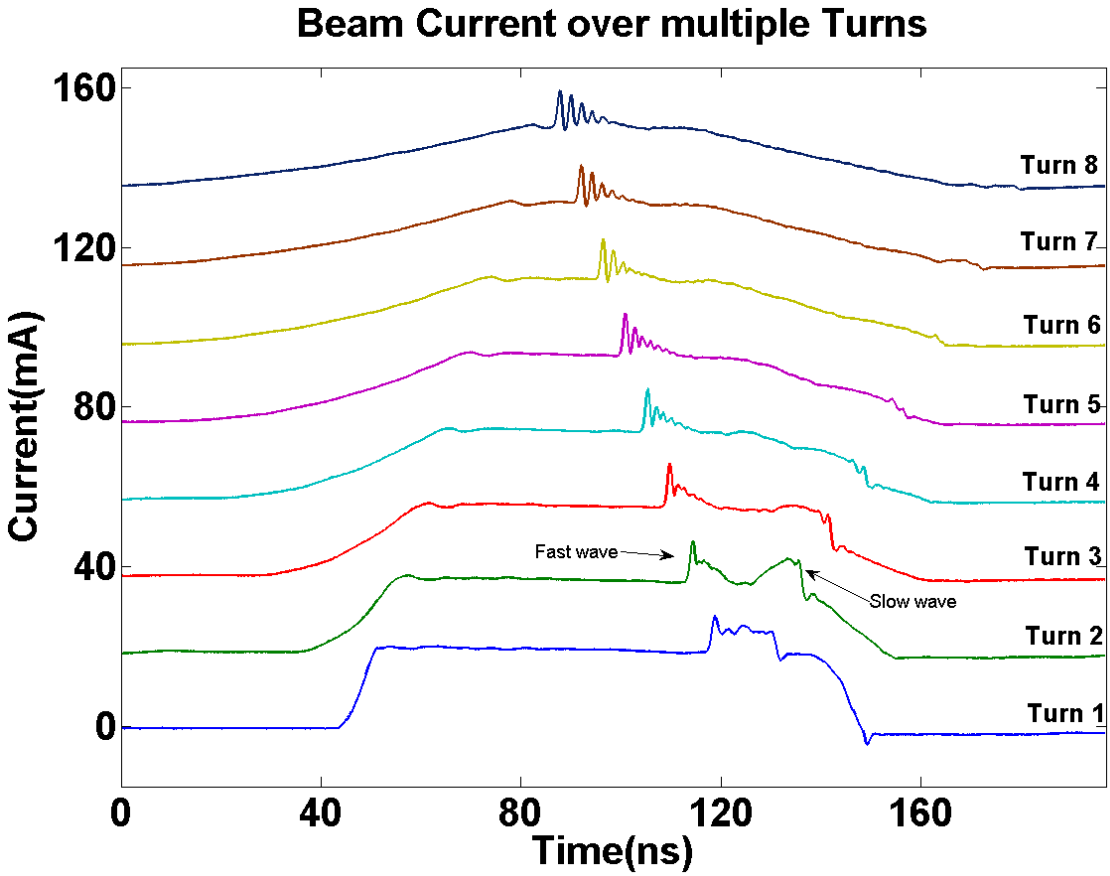

Figure 3.2: Turn-by-turn plot of beam propagation at wall current monitor (RC10), for a 22 mA beam and a 50% perturbation.

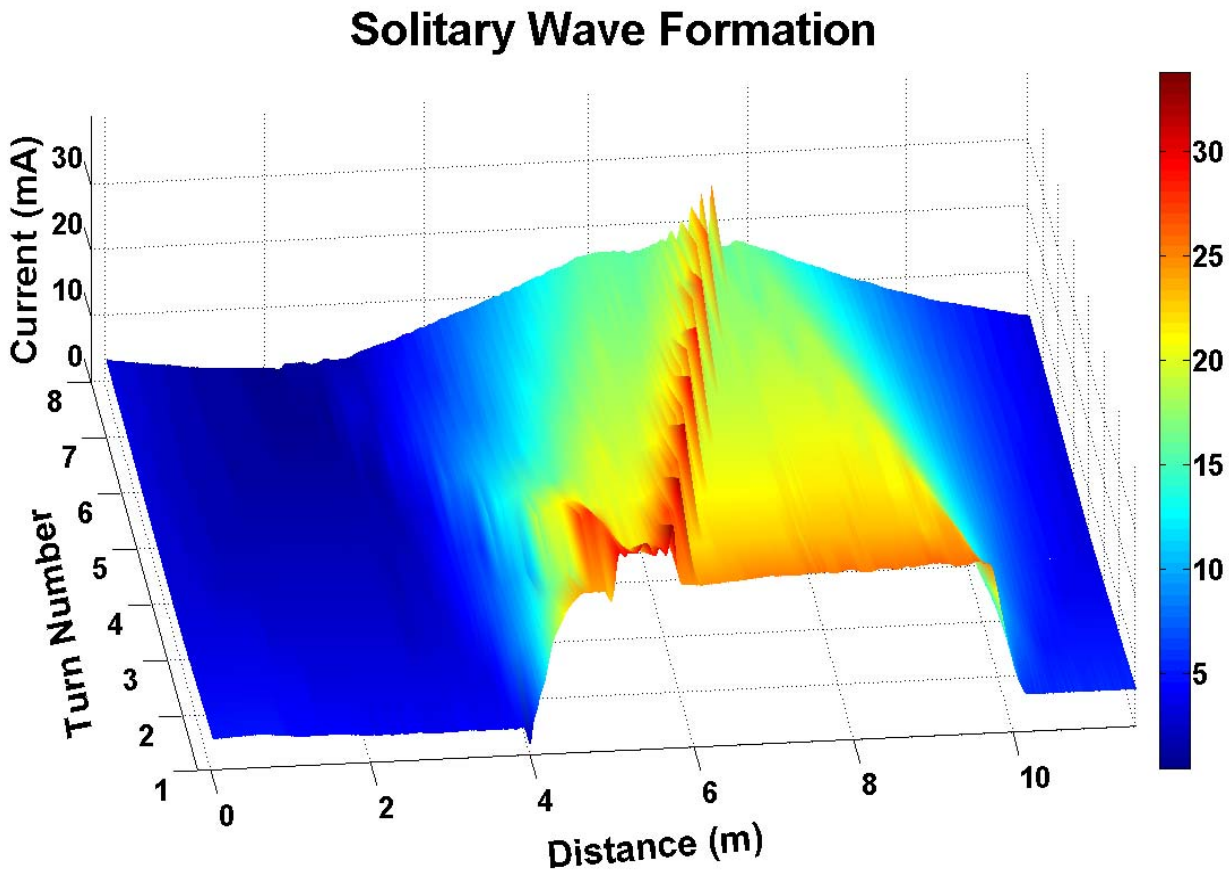

Figure 3.3: 3D Turn-by-turn plot of beam propagation at wall current monitor (RC10) , for a 22 mA beam and a 50% perturbation.

3.2 Data Analysis and Comparison to Theory

In this section, we analyze in detail the results of the experiment presented in Sec. 3.1 (22 mA, 50% perturbation). Results of the experiments presented in subsequent sections can be similarly analyzed and all show evidence of soliton behavior. A solitary wave has the property that it maintains its shape over a long distance, i.e., constant width and constant amplitude. As we illustrate in Fig. 3.4, the sub-pulse maintain its shape, within the measurement errors.

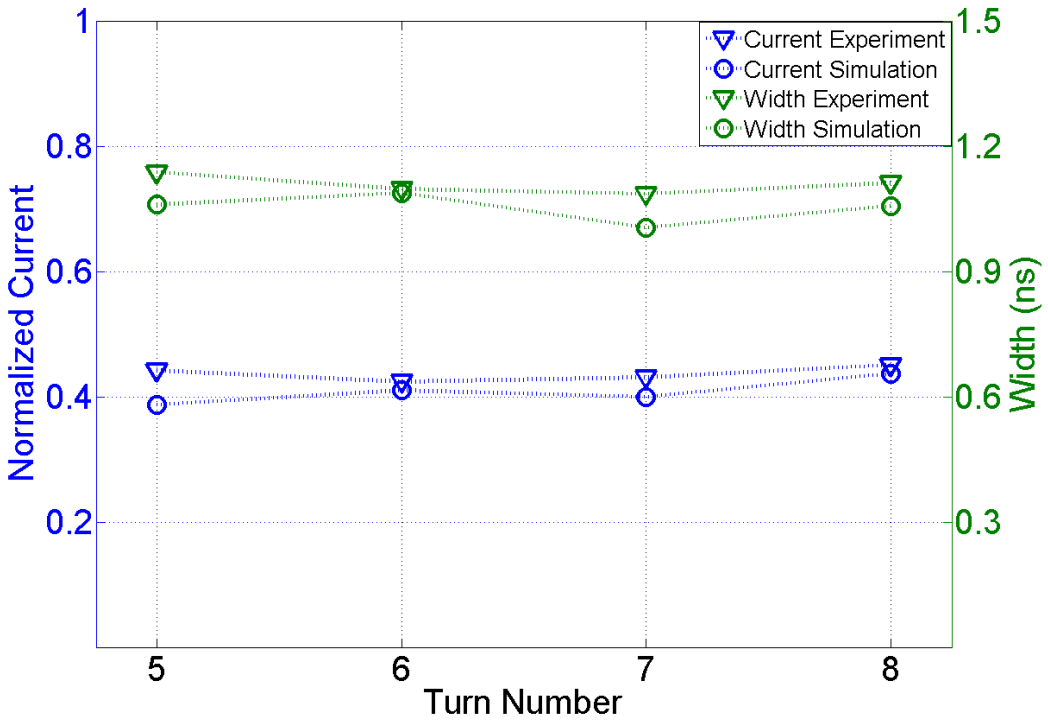

Figure 3.4: Soliton width and amplitude at different turns in the ring with both experimental and simulation data, from the 1st sub-pulse of the 22mA 25% perturbation experiment. Data points from turn 1-4 are dropped since the solitary wave train is not fully generated.

At the same time, the KdV solitons have a solution in the form of Eqn. 1.4, from which we can see that the width ($\propto 1/\sqrt{c}$) of the soliton is inversely proportional to the square root of its velocity (c), while the soliton velocity is proportional to the amplitude. From these two conditions we expect: **width^2 * amplitude = constant**. The experimental results agree with this relation, as shown in Figs. 3.5 and 3.6.

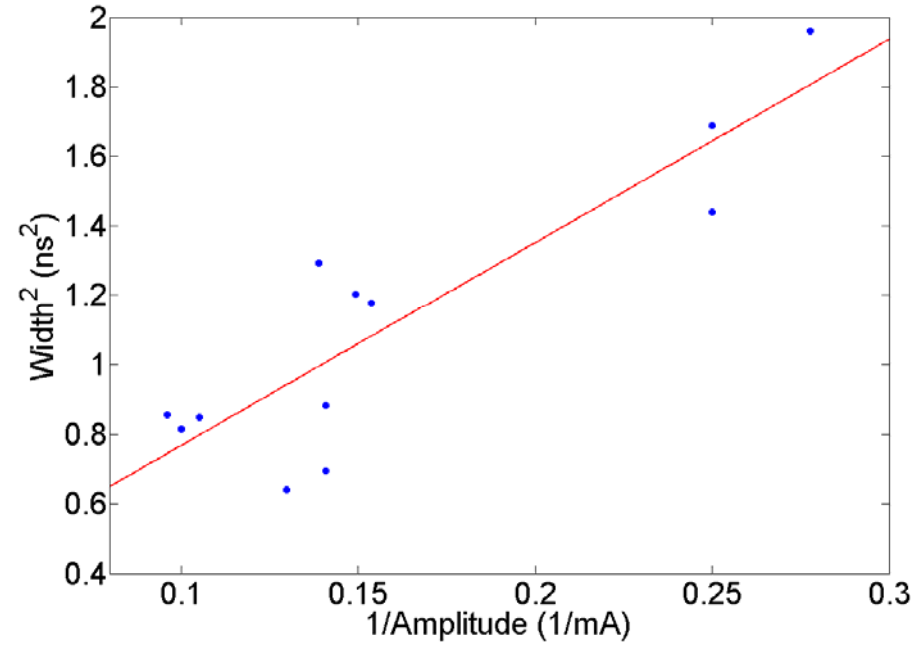

Figure 3.5: Plot of solitary wave's width^2 vs 1/Amplitude, along with its linear fit. The data points are from the 1st and 2nd sub-pulses of the wave train at 5th, 6th and 7th turn of the 22mA 25% perturbation, and 22mA 50% perturbation experiment, respectively.

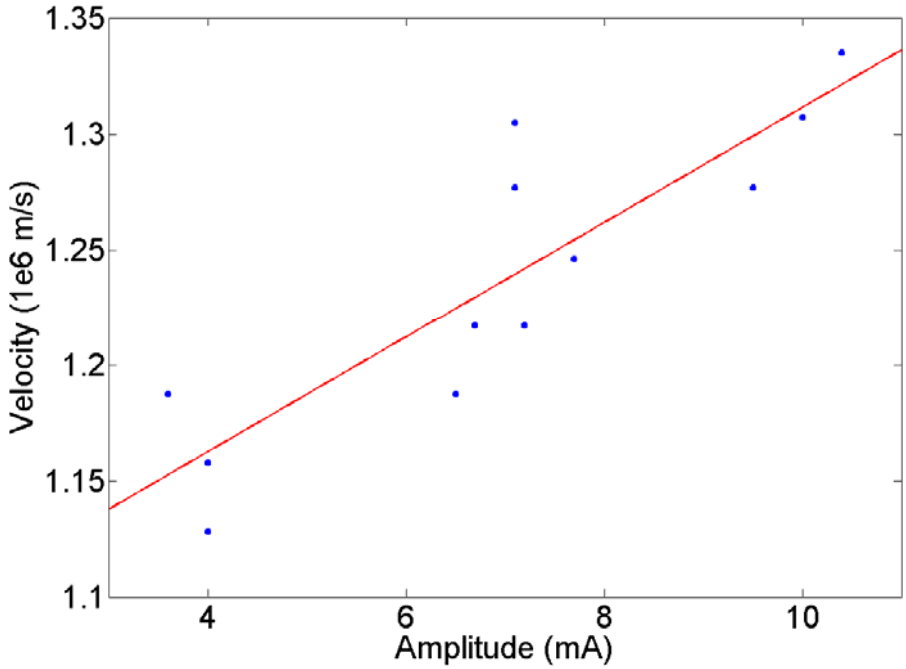

Figure 3.6: Plot of soliton velocity vs Amplitude, along with its linear fit. Same data points with the ones in Figure 3.5.

Due to the beam mismatch at the injection, there's about 10% beam loss from Bergoz to wall current monitor at the first turn, and 5% loss per turn thereafter. It will decrease the sound speed of the perturbation and may cause errors to its amplitude and width. Better beam matching and steering solution are expected for future soliton experiments. The beam loss profile is shown in Fig. 3.7:

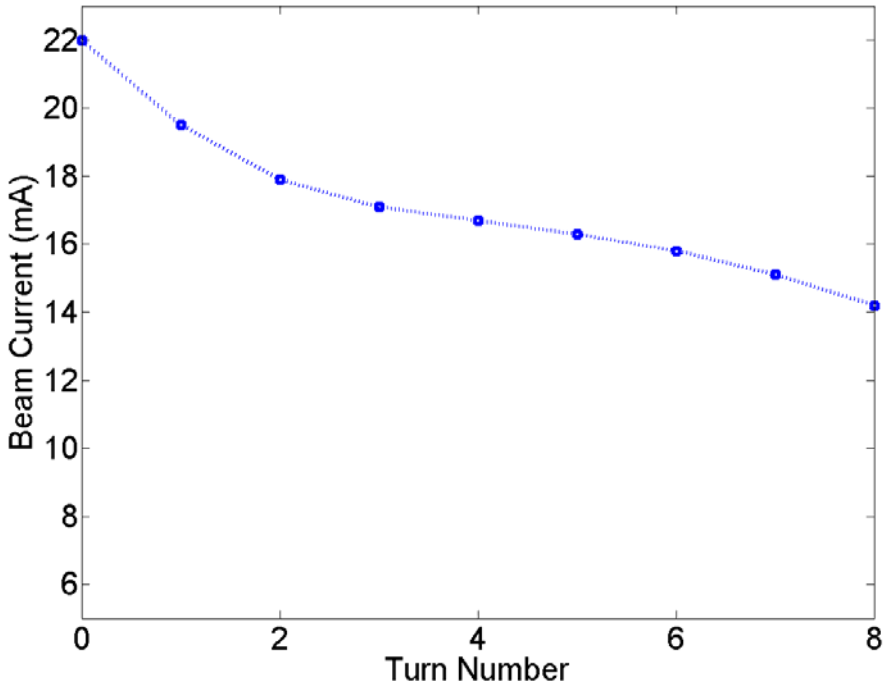

Figure 3.7: Beam current for each turn at wall current monitor (RC10), turn 0 represents the initial condition measured at Bergoz.

3.3 Soliton Dependence on Beam and Perturbation Parameters

In this section, we are interested in addressing the conditions under which solitary waves will be generated and how their evolution depends on beam parameters. We therefore systematically vary the beam current, perturbation strength and width.

In Fig. 3.8, we compare solitary waves for two different beam currents, 23mA vs. 30mA, keeping the same pulse width (about 5 ns) and relative perturbation level (20%).

The 30 mA pulse steepens faster and more sub-pulses are generated. We expect the faster propagation, since, from the linear theory at least, the sound speed is proportional to the square root of the line charge density (see Eqn. 1.1). We observed that, if the beam current is below certain threshold value (around 20 mA in UMER), then no solitons could be generated.

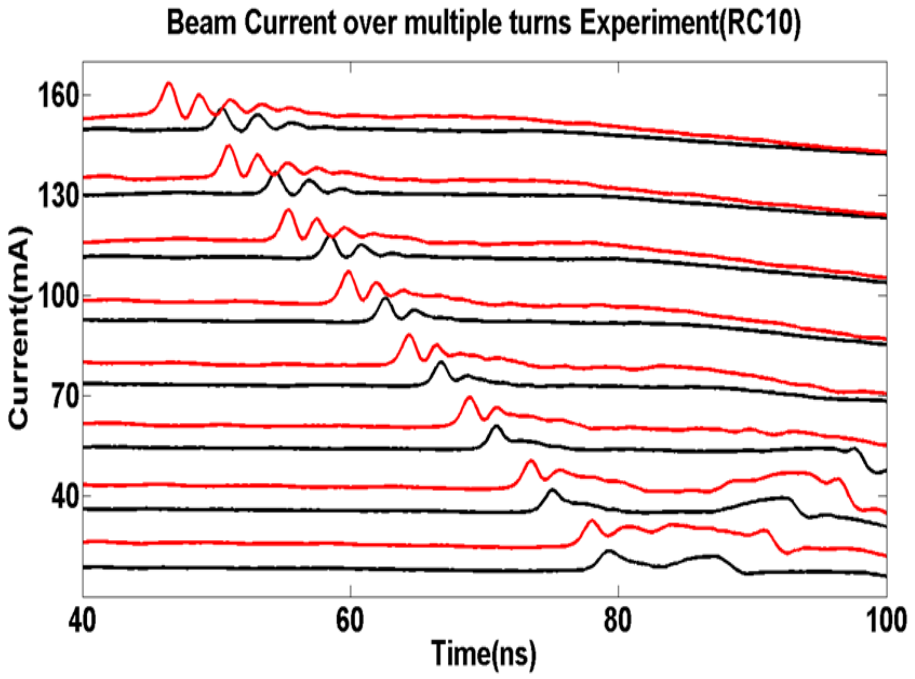

Figure 3.8: Turn-by-turn plot comparison between 23 mA beam (black) and 30 mA beam (red), both with 20% perturbation and 5 ns width.

Next, we studied the perturbation amplitude dependence. As can be seen from Fig. 3.9, different perturbation levels affect the result. The 50% perturbation case propagates faster and gives many more sub-pulses compared with the 20% perturbation case. It is consistent with the relation that a stronger pulse leads to a faster propagation speed.

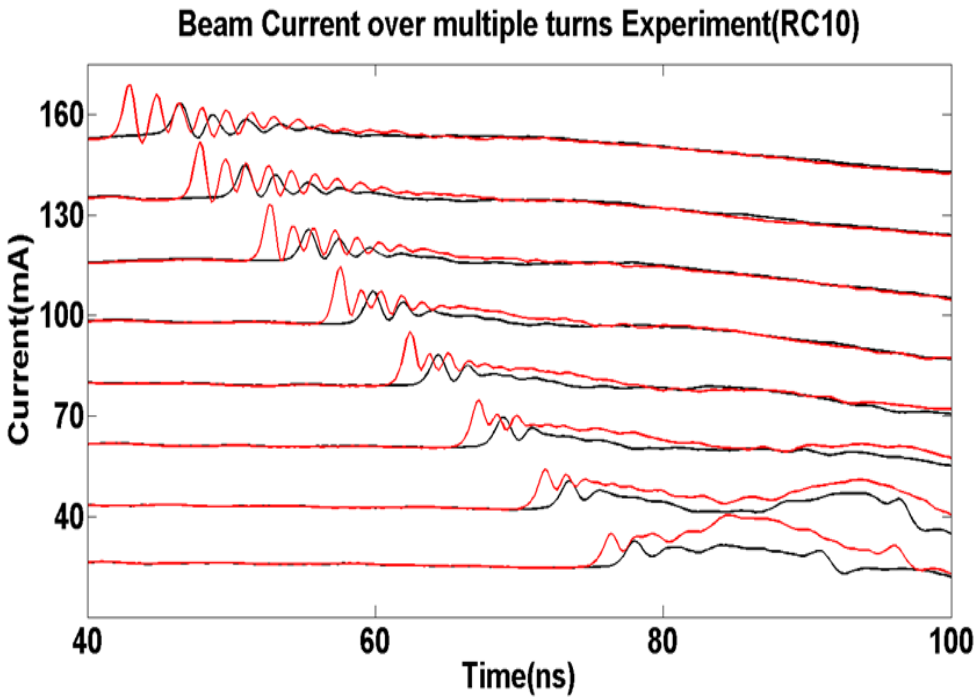

Figure 3.9: Turn-by-turn plot comparison between a 20% perturbation (black) and a 50% perturbation (red), both with 30mA main beam and 8 ns width.

In Fig. 3.10, we show different perturbation pulse widths, one 5.6 ns, the other 7.6 ns. Since they have the same beam current and perturbation level, their sound speed is very close. However, the wider pulse results in more sub-pulses, which can be explained by a diminished dispersive effect. Also, each of the sub-pulses generated from the wider pulse are stronger than the ones from the narrower pulse.

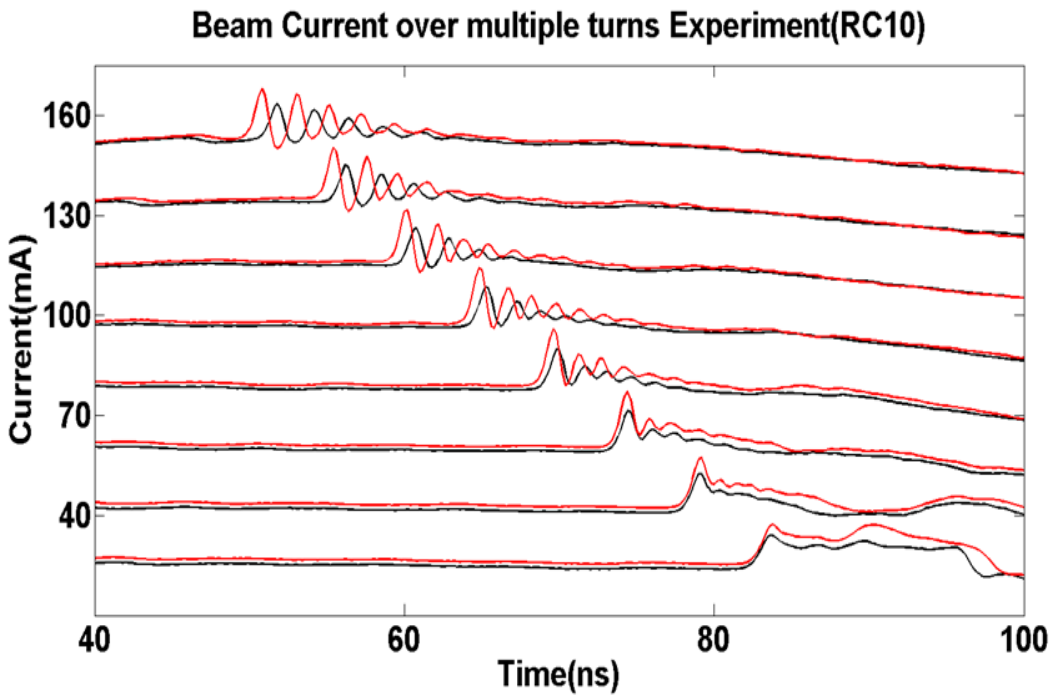

Figure 3.10: Turn-by-turn plot comparison between a 6 ns wide perturbation (black) and an 8 ns wide perturbation (red), both with a 30 mA beam and a 50% perturbation amplitude.

All the results of the soliton dependence experiments agree qualitatively with the theory. Additional studies are needed in the future to permit a more quantitative analysis.

3.4 Soliton Interactions and Two-Perturbation Experiments

In the above discussion, we have shown that the large amplitude waves we have generated satisfy the description of a solitary wave. In order to demonstrate that they are solitons, we need to further show that they behave like particles, i.e., they retain their properties after mutual interactions, or "collisions", except for a phase shift [32]. I have conducted experiments with two perturbations. I use two lasers to generate perturbations on both sides of the beam, and let the fast wave from one approach the slow wave from the other and interact with it [Fig. 3.11]. To allow enough time for the two perturbations to propagate and break before they collide, I extend the beam duration from 100 to 140 ns.

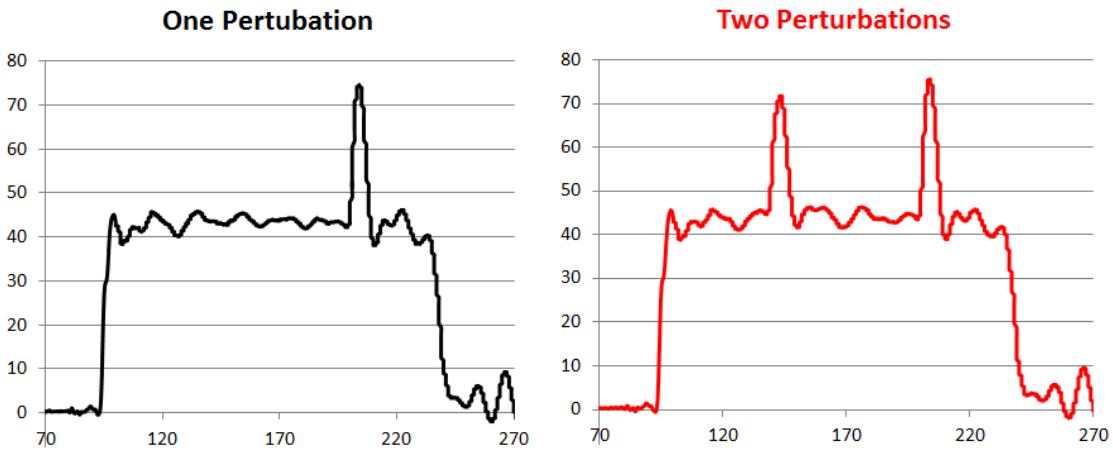

Fig. 3.11: The initial conditions for one perturbation (left) and two perturbations (right), with identical beam background (40? mA), and a same perturbation on the right edge.

Fig. 3.12 illustrates the evolution of two cases: a single 50% perturbation on a 30 mA beam (black), and the same perturbation on the same beam with the addition of another 50% perturbation on the opposite side (red). The black curve shows the fast wave of the perturbation on the right steepening and forming a soliton wave train, as above. The red curve shows the same soliton wave train going through the wave train formed by the slow wave of the perturbation initially on the left. The fact that the two curves are nearly identical for the fast wave past the interaction point is strong evidence that it is a soliton.

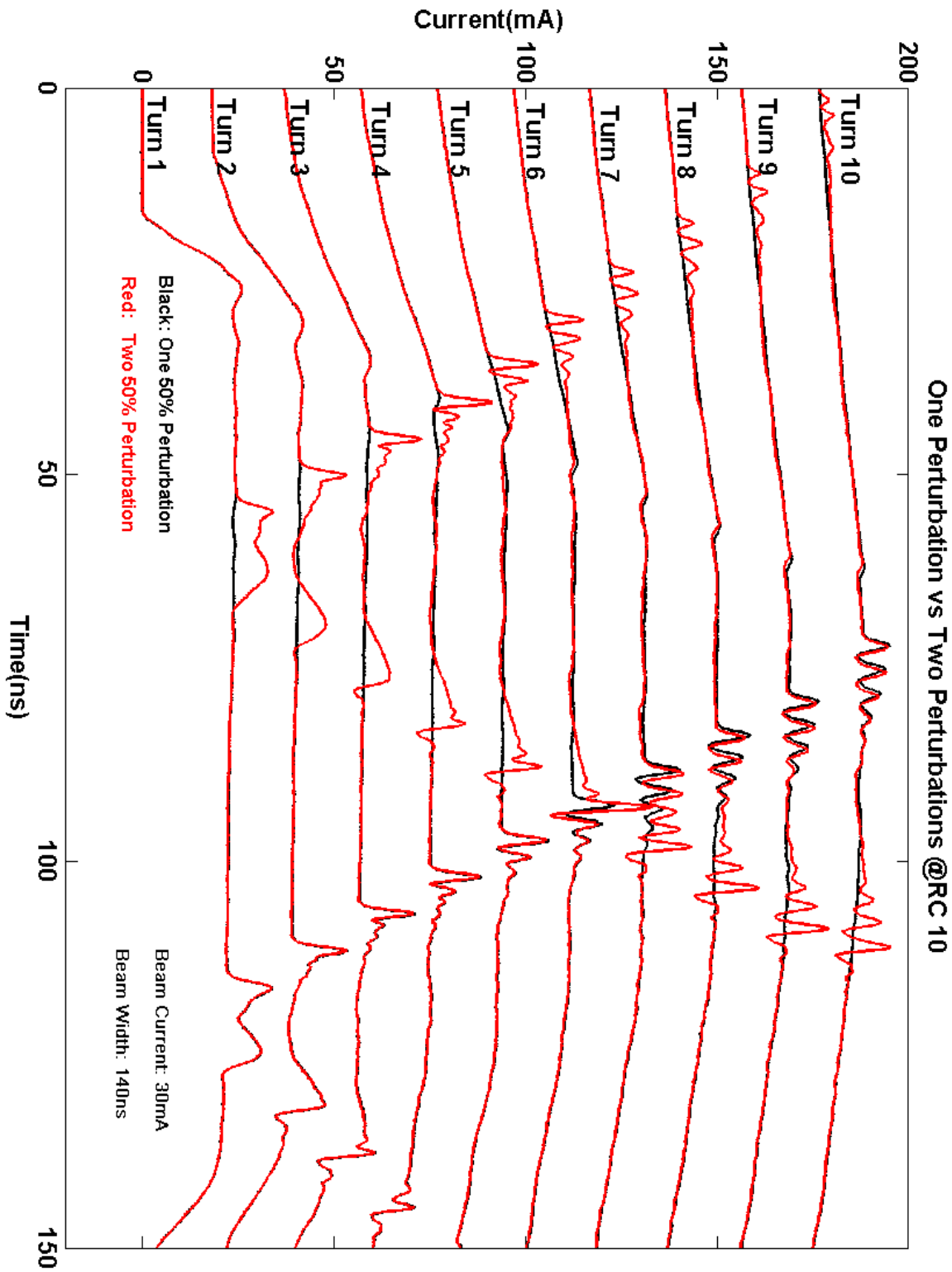

Fig. 3.12: Comparison of two-perturbation experiment and one-perturbation experiment. The fast wave of the right perturbation interact with the slow wave of the left perturbation (red), is compared with the fast wave propagation of the one perturbation case (black).

3.5 Simulation

In this section, we present the results of simulations and comparison it with the experiments. We use the R-Z model of the WARP particle-in-cell (PIC) code [33] to simulate the evolution of the beam, including the perturbation. Take the 22mA 25% perturbation case for example. We use uniform transverse focusing to represent the FODO lattice, choosing a focusing strength $\kappa = 13.33m^{-2}$ to give us the same phase advance per period (see Table 2.1). We load an initial distribution with the same measured current profile at the Bergoz. Transversely, we use a semi-Gaussian distribution, which is uniform in space and Gaussian in velocity space with uniform temperature. The initial transverse beam radius is chosen to be 9.5 mm with zero slope so it will be matched to the lattice for the beam parameters. The kinetic energy is 10 keV with a longitudinal thermal spread of 5e4 m/s. The thermal spread used is somewhat higher than what we expect for the UMER beam, mostly for the purpose of suppressing the gridding instability. However it cannot be too high or else the thermal spread will wash out the soliton structure. We found the simulation converges for the following numerical settings 4,000,000 macroparticles; a time step of 1 ns; 64 cells in R direction and 2048 cells in z direction. The grid size is 0.0254 m in R and 11.52 m in z.

Due to the beam loss in experiment, the sound speed becomes slower and so is the edge erosion rate, which has to be counted in simulation. Variable top.pgoup.sw describes the species weight (# of real particles per simulation particle). A beam loss is set by decreasing top.pgoup.sw uniformly turn by turn. When doing the calculation of beam loss from experimental data, we need to count in the inductance compensation for

the current. Check ref. [34**]** for details. Otherwise, there will be more beam loss than it actually is.

For more numerical settings and a description of the WARP code, see ref. [35].

The initial condition (beam density profile) is rather tricky. We start with the beam current profile (assuming velocity profile uniform, thus density $\propto$ current since $I = v\lambda$) measured at Bergoz, and barely get any agreement on the pulse propagation. As can been seen in fig. 3.17-3.18, with the same initial profile, the fast and slow wave in experiment (red) is much stronger than those in simulation (blue), and there's discrepancy on the right beam edge.

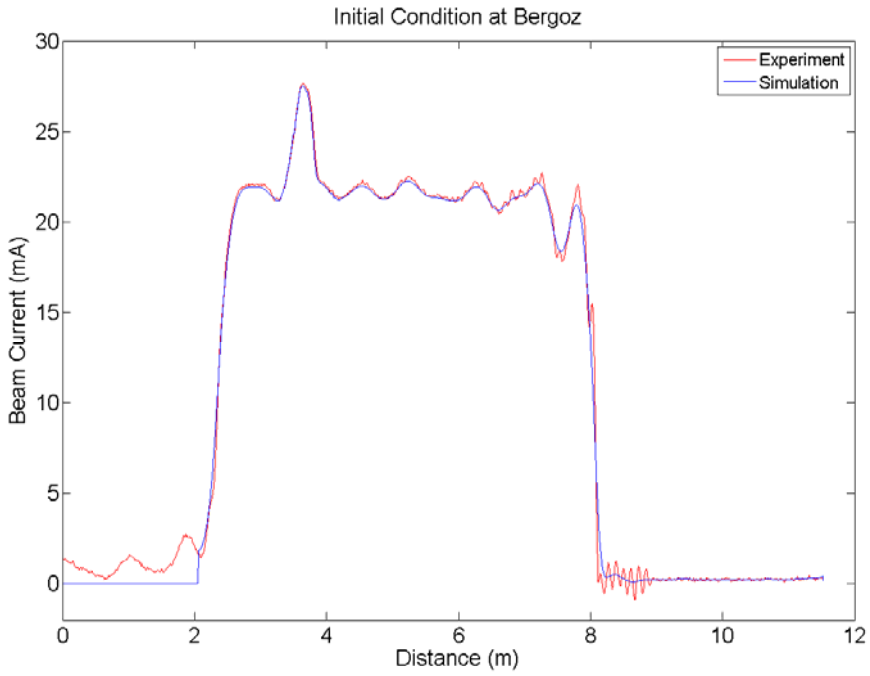

Fig. 3.13: the measured initial condition at Bergoz (red) and its smoothed profile that's imported into simulation (blue).

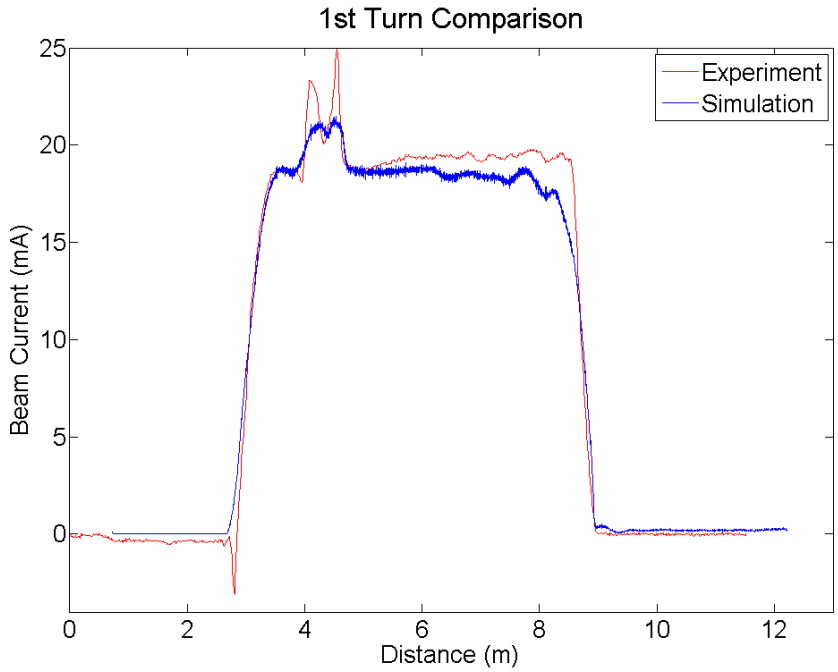

Fig. 3.14: the 1st turn comparison at wall current monitor when using the measured Bergoz current profile as the input for simulation at cathode.

Therefore, it's NOT accurate to use the Bergoz current profile as the beam right out of cathode, which could be explained from two aspects. First, there's Pulse widening during 64cm propagation. According to eqn (3.4) of [36]: $Cs = \frac{\delta t}{2\Delta z} v^2$ (3.1)

Where Cs is the sound speed, δt is the time difference between the fast and slow wave, Δz is the distance the beam travelled in lab frame, and v is beam velocity. We get $\delta t = \frac{2\Delta z Cs}{v^2} \sim$ 2*0.64*1.25e6/(6e7)^2=0.44ns, which means that the pulse widens about 0.44ns from cathode to Bergoz.

Secondly, after 64cm propagation, there comes a velocity modulation on the beam, which also contributes to the current profile, and makes it even wider. In other words, the density profile for simulation input at the cathode should be narrower. Fig. 3.15 (a-d) gives a numerical example of how energy (velocity) perturbation affects the beam pulse.

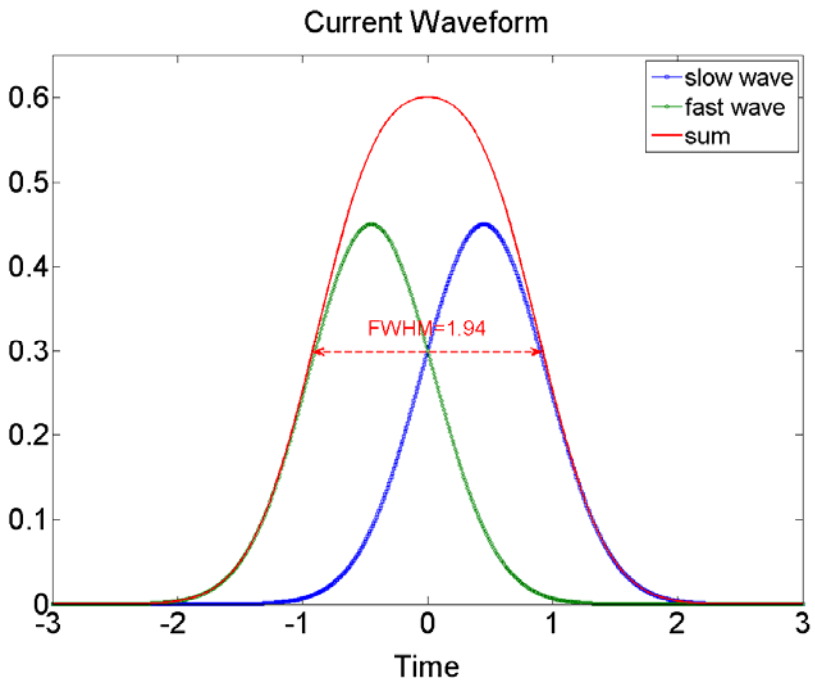

Fig. 3.15a: A numerical example of two Gaussians and their sum, as the current waveform at Bergoz.

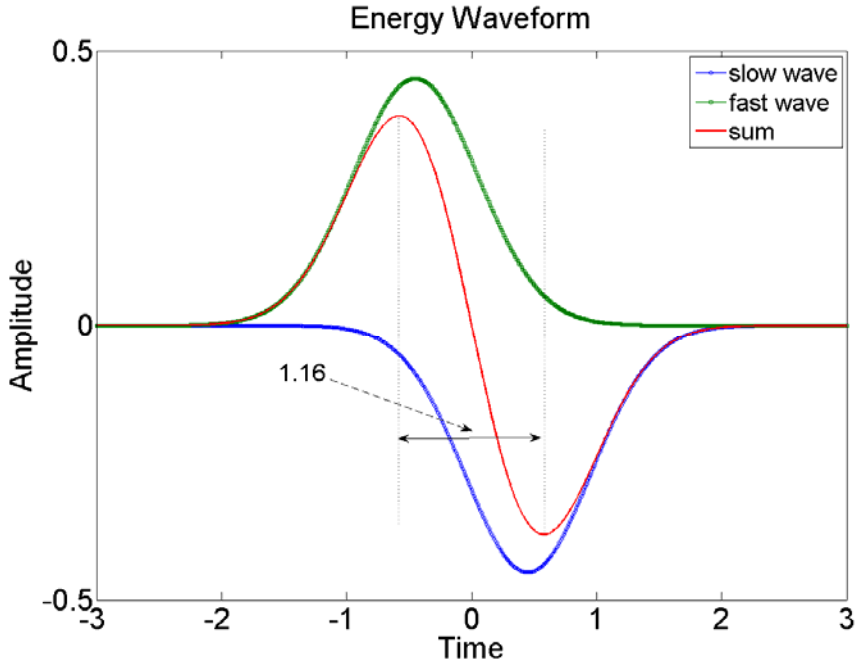

Fig. 3.15b: Switch the polarity of the slow wave, to get the energy waveforms at Bergoz.

Adjust the base level of the current and energy waveform. Say we have 20% current perturbation, set the base beam at 3 since the beam peak is 0.6 (arbitrary unit) in Fig. 2. Move the energy profile upward by 10, then we get 4%

energy perturbation (2% velocity perturbation). Dividing the current waveform by the energy waveform, we get the density profile. Compared with fig. 3.15a, the density profile is narrower than the current profile. Also, the more energy perturbation is, the narrower the width of the density profile.

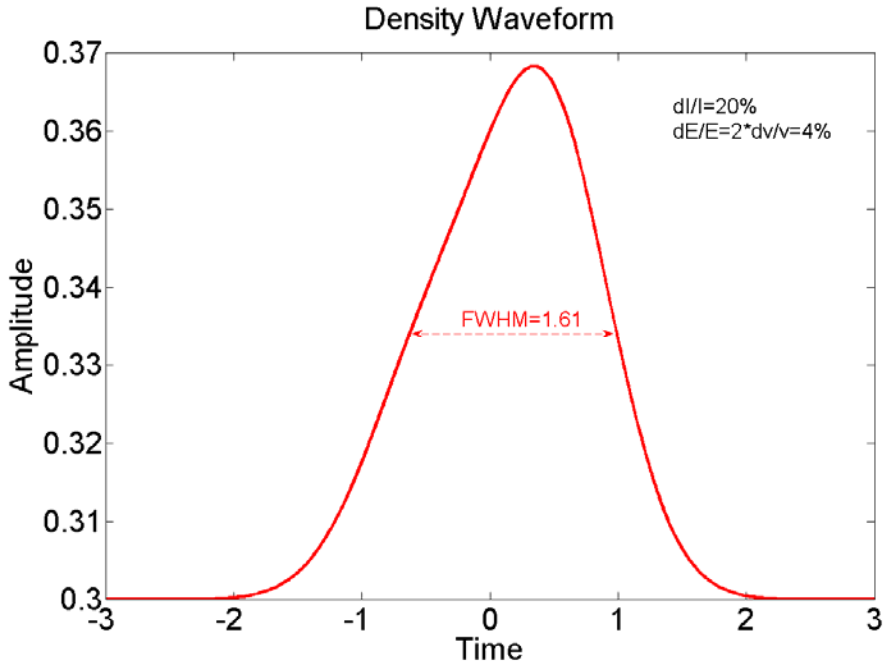

Fig. 3.15c: A numerical example of the density profile when dI/I=20%, dv/v=2%.

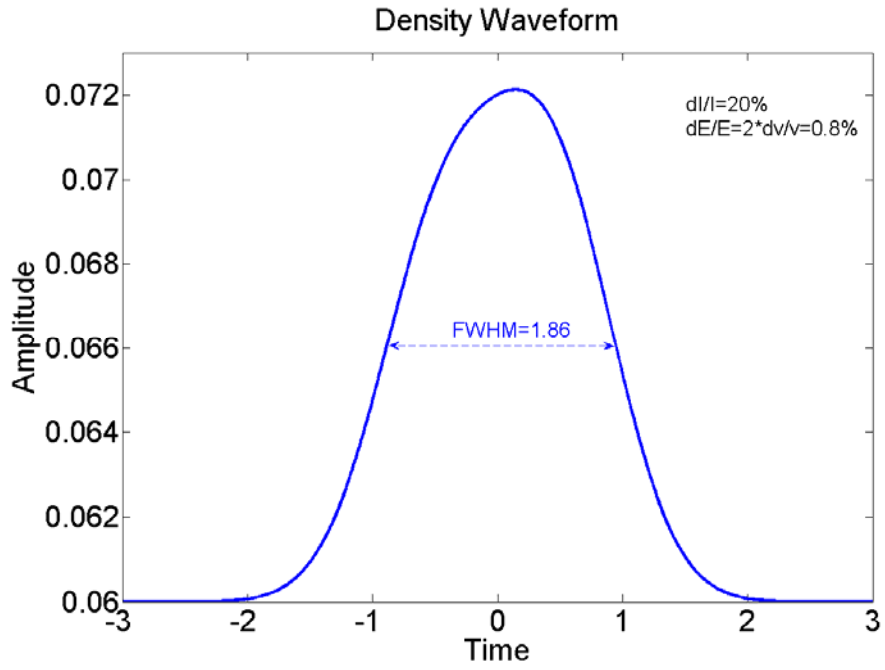

Fig. 3.15d: A numerical example of the density profile when dI/I=20%, dv/v=0.4%.

Therefore, we should either change the initial profile into some stronger/narrower perturbations, or still use the Bergoz profile, but add the velocity modulation into the code. Since we do not currently have energy analyzer installed in UMER (is under plan to be installed at IC1 in fall 2012), so we resort to starting the simulation from the cathode with an adjusted current profile (see Fig. 3.16).

In Fig. 3.16, the initial condition is assumed to be a rectangular beam with a 11mA 3.7ns wide pulse atop, compared with ~6mA 5ns perturbation in Bergoz. The intial condition adjustment leads to a good agreement between simulation and experiment at the wall current monitor. Fig. 3.17 shows the 1st, 2nd, 5th and 8th turns comparison.

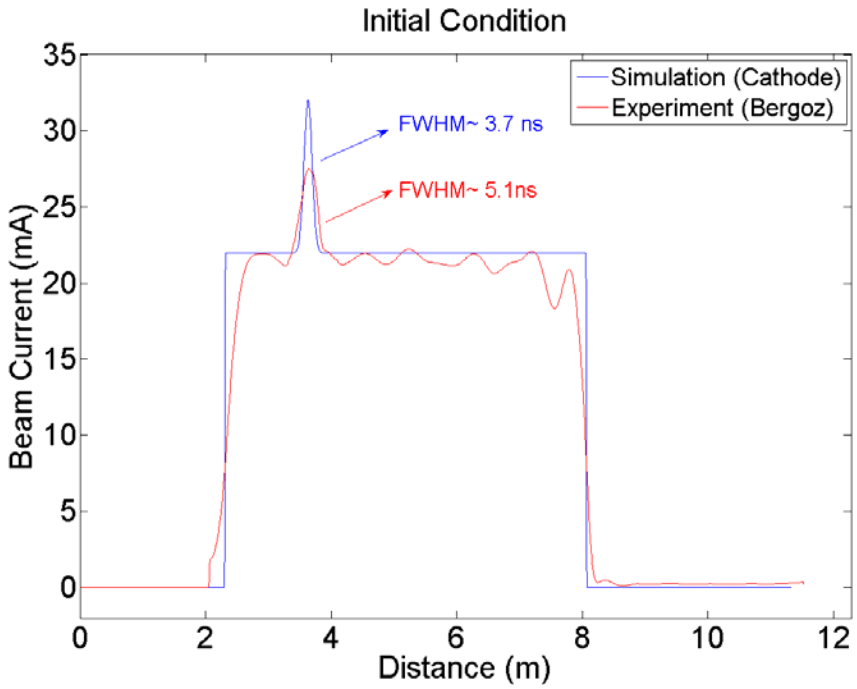

Fig. 3.16: Initial condition measured at Bergoz (red) and the modified profile (blue) imported into the cathode, for the 22 mA and 25% perturbation experiment at Bergoz.

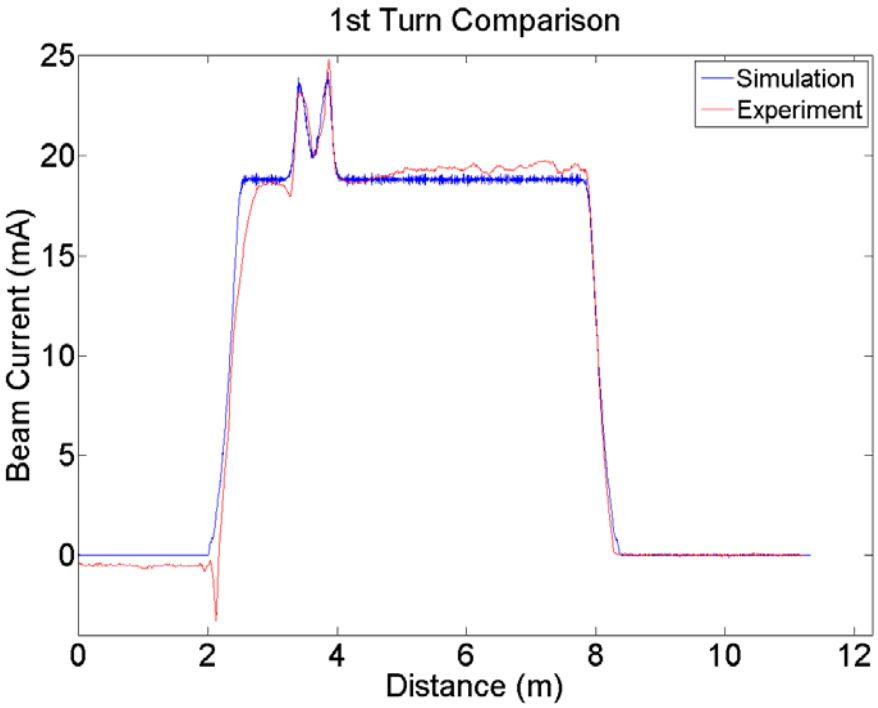

Fig. 3.17 (a): Beam current comparison between experiment (red) and simulation (blue) for the 1st turn at wall current monitor (RC10).

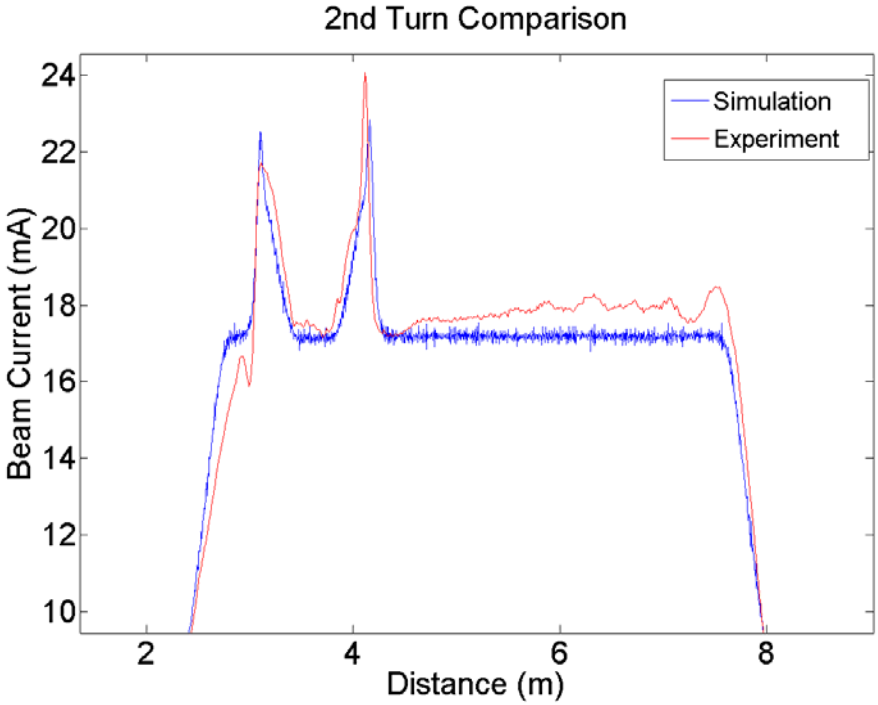

Fig. 3.17 (b): Beam current comparison between experiment (red) and simulation (blue) for the 2nd turn at wall current monitor (RC10).

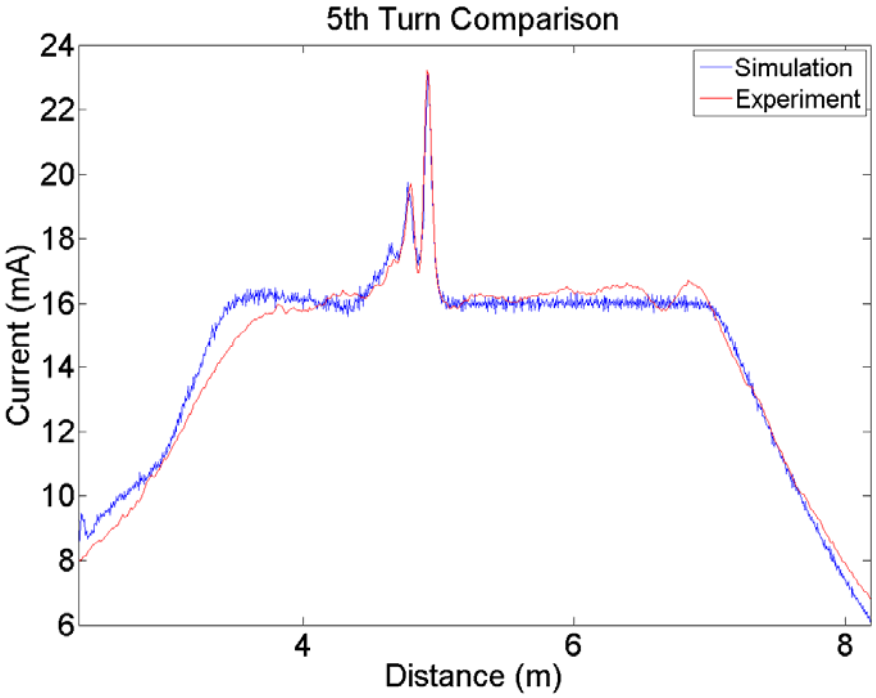

Fig. 3.17 (c): Beam current comparison between experiment (red) and simulation (blue) for the 8th turn at wall current monitor (RC10).

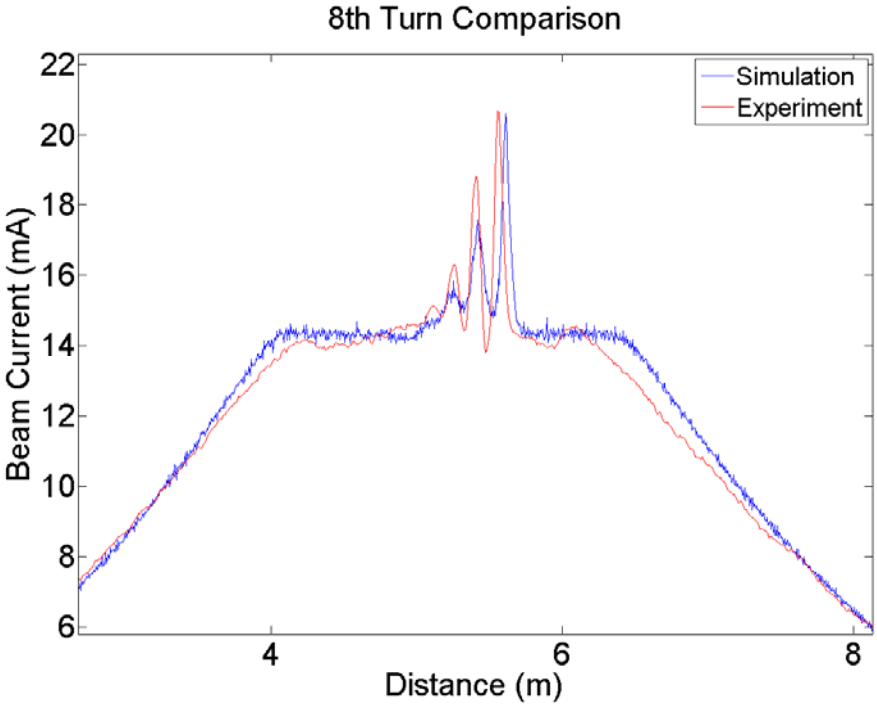

Fig. 3.17 (d): Beam current comparison between experiment (red) and simulation (blue) for the 8th turn at wall current monitor (RC10).

The agreement is not perfect and it depends on several aspects. First, the initial beam could be not ideally rectangular due to a response time at the thermionic dispenser, which results in a little discrepancy on the edge erosion, as shown in Fig. 3.17(c). Secondly, the initial perturbation pulse is not necessarily Gaussian, and the profile difference may lead to a slight disagreement on the amplitude and width of the sub-pulses in the soliton wave train. Thirdly, the beam loss affects the longitudinal dynamics a lot, which we assume to be uniform in simulation but might not be the case in experiment, especially right after the injection due to the initial beam mismatch; In addition, there are also parameters like beam radius and emittance that we made a reasonable guess based on the experimental data taken at different chambers of the alternating-gradient ring, while we assume uniform focusing in simulation. Despite all those factors above, the overall agreement between simulation and experiment is reasonable.

For better guidance in furture simulations, a table describing the beam variables' sensitivity to longtitudinal dynamics is as follows:

Table 3.1 Variable sensitivity to beam dynamics in WARP

Variables	Sensitive or not	Affect
Beam current	Yes	erosion rate, soliton speed
Average Beam radius	Yes	erosion rate, soliton speed
Perturbation shape	Yes	soliton speed, wave train form
Emittance	No	N/A
Long. Thermal Spread	No	numerical stability
Env. radi as function of dist.	No	N/A

3.6 Summary

We have shown the formation of soliton wave trains in electron beams, both in experiment and simulation. We also explore the soliton dependence on beam current, perturbation strength and width. The experimental result reproduced by WARP simulation.

Chapter 4: Conclusion

4.1 Summary

To sum up, I report in this thesis the experimental observation of a soliton wave train on intense electron beams by deliberately introducing large-amplitude density perturbations. In addition to demonstrating that the observed waves are solitons, I find that, to generate solitons, the main conditions are a sufficiently high beam space charge intensity, a large perturbation amplitude (usually >20%), a long enough propagation distance (~10 times the perturbation length in the beam frame), and a relatively wide perturbation pulse (a few times of the pipe radius). An advantage of studying solitons on particle beams in UMER is the ability to generate solitons over a wide range of parameters, to control the propagation precisely and track them for a long distance. We complete the first soliton characterization by modifying beam current and perturbation strength and width.

The results agree reasonably well with theory and simulation, though it is not perfect. We expect the results to improve as ongoing efforts to optimize the UMER steering and matching result in reduced beam losses. The results are scalable to larger accelerators, provided the relative strengths of space charge to external forces are the same.

4.2 Future Plans

Worthwhile future investigations can be: to study soliton reflection at the beam end in the presence of induction focusing, currently the wave train will step off the beam edge; generation of solitons from initial velocity modulations (using the induction cell to

modulate velocities), which could be used for beam cancellation since the velocity perturbations lead to negative waves; and taking the wall impedance into consideration. Another topic could be the effect of beam transverse distribution on the soliton characteristics. The current theoretical/simulation model is based on certain distributions like Gaussian, Bessel function, and waterbag distribution. By using the DMD mirror [37] to selectively reflect the drive laser, we will be able to generate any transverse distribution.

We suggest that solitons can be used to modulate an electron beam for a tunable, coherent THz radiation source. The bunch spacing can be varied with a velocity tilt or a chicane.

Appendix A: Laser Alignment Procedure

This appendix gives the key procedures for doing the laser alignment in the beam perturbation experiment using photoemission.

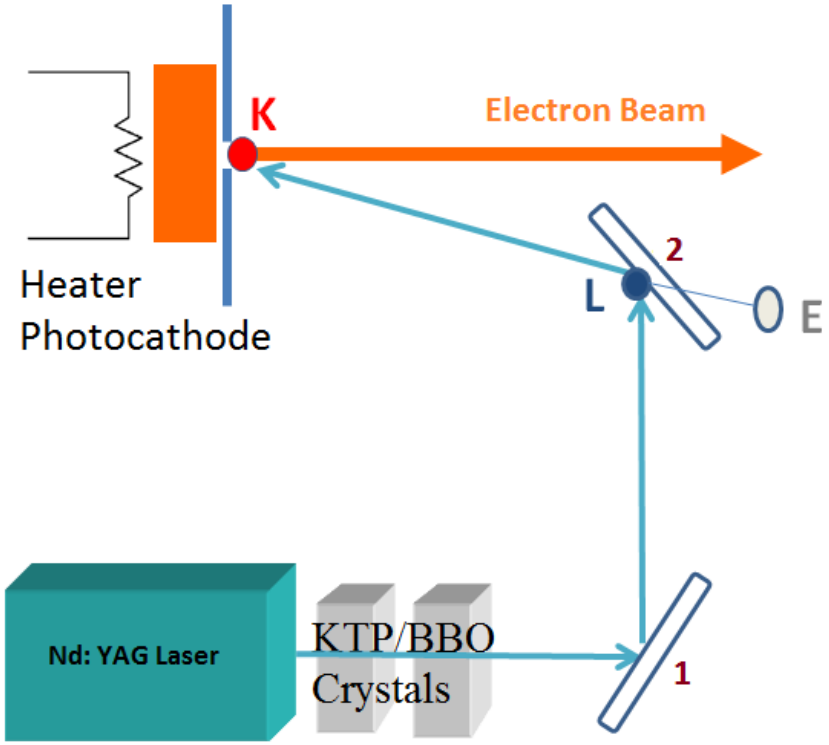

1. Adjust dielectric mirror 2, make sure the eye (E) could see the cathode (K) through the center (roughly) of the mirror;
2. Adjust dielectric mirror 1, reflect the laser to hit around the center (L) of mirror 1, and make the 2nd reflection toward the cathode(K) as close as possible by fine adjustment of mirror 1;
3. Do fine adjustment of mirror 2, make E, L, and K on the same line, which ensures that the laser hits right at the cathode.

Appendix B: WARP Code for Soliton Simulation

```
comment  =  """ Soliton Train - 22+11 mA """
from warp import *         # --- import warp
from lwplots import *      # --- import laboratory frame window plots
from  monitor import *     # --- import ability to change run at execution
import string

# createmonitor(passwd="mo$job", port = 50008) # --- used for real time monitor
setup(runcomments=comment, cgmlog=0)

beam_curr     = 0.022
pert_curr       = 0.011


top.ekin         = 10000      # beam energy in volts
top.ibeam      = 0.033     # not actually used except fort matching
top.a0           = 0.0095635933729712099  # matched value for dedr at 22mA+11mA
top.b0          = top.a0
#top.dedr      = -271976.137 # caculated value for tune=6.67
top.dedr        = -115576.36079661094
top.emit        = 35.0e-06
top.ap0         =  0.
top.bp0         =  0.
top.zion        =  1.0e0             # use positive electrons for simplicity
top.aion        =  top.emass/top.amu  # electron mass
top.lrelativ    =  false             # nonrelativistic (in beam frame.)
w3d.xmmax       =  0.0254            # System size in x (actually r)
w3d.ymmax       =  w3d.xmmax
top.rwall       =  w3d.xmmax         # Pipe radius
w3d.solvergeom =  w3d.RZgeom         # Set solver to R-Z gemetry

#  --- calculate beam velocity to set length use same algorithm as in code
if (top.lrelativ):
   kk          = top.jperev*top.ekin/(top.aion*top.amu*top.clight**2)
   gg          =  1.e0 + kk
   v_beam      =  clight * sqrt((2*kk+kk**2)/gg**2)
else:
   v_beam      =  sqrt( (2.e0*top.ekin*top.jperev/top.aion)/top.amu )

# --- Calculate beam length for a 100ns beam

beamlen        =  100e-09*v_beam
##########################################################################
#####
```

```
# --- Use envelope integrator to calculate the matched solution.
# --- Set dedr, the uniform focusing electric field (in the Larmor frame)
# --- for a matched beam

top.tunelen    =  2*beamlen
env.zl         =  -0.0
env.zu         =  3.0*beamlen
env.dzenv      =  0.001

derivqty()

package("env")
generate()
step()


#winon()               # --- turns on plot window when running interaticely

plg(env.aenv,env.zenv)

#raise()
fma()

#top.dedr=top.dedr*(1+3.*env.deltaa/top.a0);top.dedr;
#top.a0=top.a0*(1+0.5*env.deltaa/top.a0);top.b0=top.a0;top.a0;
#generate();step();fma();plg(env.aenv,env.zenv)


###############################################################################
######

#top.dt         =  0.1/v_beam    # Set timestep to beam propagating 1 cm
top.dt         =  1*ns          # Round number convenient for analysis
w3d.zmmax      =  11.52     # Set max in z
w3d.zmmin      =  0.            # Set min in z
top.zimin      =  0 #2.62           # Left edge of beam
top.zimax      =  11.52 #8.26     # Right edge of beam (Set to whole system

w3d.nx         =  64          # no of cells in R
w3d.ny         =  1           # note that y direction is not used.
w3d.nz         =  2048        # no of cells in z

#setup for vzbar vs z plot
top.nzmmnt     =  w3d.nz
top.zmmntmax   =  w3d.zmmax
```

```
top.zmmntmin   =  w3d.zmmin

#  --- Set parameters for loading Particles

top.npmax      =  4000000    # Number of particles in the simulation
w3d.distrbtn   =  "semigauss"
w3d.ldprfile   =  "polar"
w3d.vtrandom   =  "pseudo"
w3d.vzrandom   =  "pseudo"

# --- Longitudinal thermal spread.
top.vthz = 0.5e05              # This number is a guess

# --- this section used only when beam length is less than system length
#w3d.cigarld=1
#w3d.distr_l = "gaussian"
#top.straight = 0.95


#  --- Set input current waveform (importing data)- code will automatically load beam in
z


ff = open("initialcondition.csv",'r')
text = ff.readlines()
ff.close()

length_=2048

current = []   #Bergoz coil Current.

no_lines = 0

for line in text:
  no_lines = no_lines + 1
  items = string.split(line, ",")
  current.append(float(items[0]))

current = array(current)


w3d.nzdist = length_
gchange("InPart3d")
w3d.zdist  = current
```

```
# --- Set boundary conditions on particles and fields

top.pbound0    = periodic
top.pboundnz   = periodic
top.pboundxy   = absorb
w3d.bound0     = periodic
w3d.boundnz    = periodic

top.nhist = 1
top.iflabwn  = 1
top.itlabwn  = 1
top.nlabwn   = 1
top.zlw      = 12.67 #0.5*w3d.zmmax
print(top.zlw)
#top.lgridqnt = 1

package("w3d")
generate()


pzcurr()               # --- plot initial beam-frame current
fma()
#savetxt('initial.dat', (top.curr[:,0]))

#plg(top.vzbarz[:,0],top.zmntmesh)
#fma()

##STOP SIMULATION HERE IF YOU WANT TO TEST INITIAL LOADING
#kjsdkjskdjk


iiimax  = 8


#  --- Set up array to hold output currents and zmesh

currents = zeros((w3d.nz+1,iiimax+1),'d')
meshes   = zeros((w3d.nz+1,iiimax+1),'d')



#ppzx(color='density',chopped=0.1)
#fma()   # moved before the main loop, after the envelope radius setting

jjjwcm  = 7.67/(top.dt*top.vbeam)-1
```

```
jjjmax  = w3d.zmmax/(top.dt*top.vbeam)-1

sw_save = top.pgroup.sw[0]
sw0=0.9   #right out of Bergoz, a lot of loss due to mismatch?!
sw1=0.838 #1st turn at RC10
sw2=0.7773 #2nd turn at RC10
sw3=0.7091 #6th turn at RC10
sw4=0.6727 #7th turn at RC10
sw5=0.65 #8nd turn at RC10

t0=0.24/v_beam
t1=(7.67+0.64)/v_beam
t2=(19.19+0.64)/v_beam
t3=(65.27+0.64)/v_beam
t4=(76.79+0.64)/v_beam
t5=(88.31+0.64)/v_beam


iii=0

currents[:,iii] = top.curr[:,0]
meshes[:,iii]  = top.zlmesh[:]+top.zbeam

top.ncolor = 10          # 10 colors in the phase space plots


#  --- Simple program to put smoothing into field calculation
def update_bndrz():
   g = frz.basegrid
   f=g.phi
#  --- Hardwire in periodic
#   if g.izlbnd==dirichlet:f[:,0]=2.*f[:,1]-f[:,2]
#   if g.izlbnd==neumann:f[:,0]=f[:,2]
#   if g.izlbnd==periodic:f[:,0]=f[:,-2]
   f[:,0]=f[:,-2]
#   if g.izrbnd==dirichlet:f[:,-1]=2.*f[:,-2]-f[:,-3]
#   if g.izrbnd==neumann:f[:,-1]=f[:,-3]
   f[:,-1]=f[:,1]
#   if g.izrbnd==periodic:f[:,-1]=f[:,1]
# w3d.phi[:,0]=w3d.phi[:,-2]
# w3d.phi[:,-1]=w3d.phi[:,1]

def smoothz():
   s=0.5
   n=3
   ff = frz.basegrid.phi
```

```
  for i in range(n):
    ff[:,1:-1] = s*ff[:,1:-1]+(1.-0.5)*s*(ff[:,:-2]+ff[:,2:])
# w3d.phi[:,1:-1] = s*w3d.phi[:,1:-1]+(1.-0.5)*s*(w3d.phi[:,:-2]+w3d.phi[:,2:])
    update_bndrz()

#  --- force use of phi to calculate fields so that smoothing works
frz.l_get_fields_on_grid=false

installafterfs(smoothz)


#  ---  Set initial envelope radius (not uniform due to the perturbation)

jj=0

while jj < top.npmax-1:
      a=(top.pgroup.zp[jj]-top.zimin)/((top.zimax-top.zimin)/length_)
      top.pgroup.xp[jj] = top.pgroup.xp[jj] * sqrt(w3d.zdist[a]/beam_curr)
      top.pgroup.yp[jj] = top.pgroup.xp[jj]
      jj=jj+1

ppzx(color='density',chopped=0.1)
fma()




# --- Main Loop

while iii < iiimax :
  iii = iii+1
  jjj = 0
  if iii == 1:
    while jjj < jjjwcm :
     jjj = jjj + 1
     step()
     if 0<top.time < t0:
       top.pgroup.sw =  (1. - (1.-sw0)*top.time/t0)*sw_save
     if t0 < top.time < t1:
       top.pgroup.sw = (1. - ((1.-sw1/sw0)*(top.time-t0))/(t1-t0))*sw0*sw_save
     if top.zbeam > top.zlw: top.zlw = top.zlw + w3d.zmmax
  if iii > 1:
    while jjj < jjjmax :
     jjj = jjj + 1
     step()
```

```
      if 0<top.time < t0:
        top.pgroup.sw = (1. - (1.-sw0)*top.time/t0)*sw_save
      if t0 < top.time < t1:
        top.pgroup.sw = (1. - ((1.-sw1/sw0)*(top.time-t0))/(t1-t0))*sw0*sw_save
      if t1 < top.time < t2:
        top.pgroup.sw = (1. - ((1.-sw2/sw1)*(top.time-t1))/(t2-t1))*sw1*sw_save
      if t2 < top.time < t3:
        top.pgroup.sw = (1. - ((1.-sw3/sw2)*(top.time-t2))/(t3-t2))*sw2*sw_save
      if t3 < top.time < t4:
        top.pgroup.sw = (1. - ((1.-sw4/sw3)*(top.time-t3))/(t4-t3))*sw3*sw_save
      if t4 < top.time < t5:
        top.pgroup.sw = (1. - ((1.-sw5/sw4)*(top.time-t4))/(t5-t4))*sw4*sw_save
      if top.zbeam > top.zlw: top.zlw = top.zlw + w3d.zmmax

  fma()
  pzcurr()
  fma()
  pzcurr()
  limits(top.zbeam+0.66*beamlen,top.zbeam+1.33*beamlen,'e','e')
  fma()
  ppzx(color='density',chopped=0.1)  # , contours=10)   # Uncomment if you get only 5
colors
  fma()
  ppzvz(color='density',chopped=0.1)
  currents[:,iii] = top.curr[:,0]
  meshes[:,iii]  = top.zlmesh[:]+top.zbeam
  fma()
  pcurrlw(ilw=0)
fma()

# --- Text output
runid = arraytostr(top.runid)
ff1 = open(runid+".currout.txt", "w")
ff2 = open(runid+".meshout.txt", "w")
for iii in range(0, currents.shape[0]):
   for jjj in range(0, currents.shape[1]):
      print >> ff1, '%8.6f'%(currents[iii, jjj],),
      print >> ff2, '%8.6f'%(meshes[iii, jjj],),
   print >> ff1
   print >> ff2
ff1.close()
ff2.close()

savetxt('currlw.dat', (top.currlw))
savetxt('timelw.dat', (top.timelw))
savetxt('vzbarz.dat', (top.vzbarz))
```

Bibliography

[1] L. Evans. The Large Hadron Collider. *New J. Phys*, 9:335, 2007.

[2] R. R. Wilson. The Tevatron. *Phys. Today*, 10:23–30, 1977.

[3] P. Emma. The Stanford Linear Collider. *Proc. of PAC95*, **1**, 1995: 609-610.

[4] H. Winick. Fourth Generation Light Source. *Proc. of SLAC-PUB*, 1997: 37-41.

[5] T. C. Marshall, *Free Electron Laser* (Macmillan Publishing Co., New York, 1985).

[6] J. Wei et al., *Proc. of. IPAC*, Portland, OR, 2003, p. 571.

[7] T. Shaftan, and Z. Huang, Phys. Rev. ST-AB, 7, 080702 (2004).

[8] J. G. Wang, D. X. Wang, and M. Reiser, Phys. Rev. Lett. **71**, 1836 (1993).

[9] K. Tian, R. A. Kishek, I. Haber, M. Reiser, and P. G. O'Shea, Phys. Rev. ST-AB,13, 034201 (2010).

[10] J. Bisognano, I. Haber, L. Smith, and A. Sternlieb, IEEE Trans. on Nucl. Sci. 28, 2513 (1981).

[11] R. Davidson, Phys. Rev. ST-AB, **7**, 054402 (2004).

[12] S. Ramo, Physical Review, **56**, 276, (1939).

[13] W. C. Hahn, Gen. Elec. Rev., **42**, 258, (1939).

[14] C. Birdsall and J. Whinnery, Journal of Applied Physics, Vol. **24**, 3, 314, (1953).

[15] D.X. Wang, J.G. Wang, and M. Reiser, Phys. Rev. Lett., **73**, 66, (1994).

[16] H. Suk, J. G. Wang, and M. Reiser, Phys. Plasmas **3** (2), 669 (1995)

[17] Y. Huo, Masters Thesis, University of Maryland, (2004).

[18] J.R. Harris, J.G. Neumann and P.G. O'Shea, Journal of Applied Physics, 99, 093306, (2006).

[19] J. C. T. Thangaraj, Ph.D. Dissertation, University of Maryland, (2009).

[20] Scott Russell, J., *"Report on waves"*. Fourteenth meeting of the British Association for the Advancement of Science. (1844)

[21] N. J. Zabusky and M. D. Kruskal, Phys. Rev. Lett. **15**, 240 (1993).

[22] H. Ikezi, R. J. Taylor and D. R. Baker, Phys. Rev. Lett., **25**,11-14 (1970)

[23] H. Schamel, Phys. Rev. Let. **79**, 2811 (1997)

[24] M. Blaskiewicz, and J. Wei, Phys. Rev. ST-AB, **7**, 044402 (2004).

[25] S. Koscielniak, S. Hancock and M. Lindroos, Phys. Rev. ST-AB, **4**, 044201 (2004).

[26] M. Reiser, *Theory and Design of Charged Particle Beams* 2nd Ed. (Wiley-VCH Inc., Weinheim Germany, 2008).

[27] http://panda.unm.edu/Courses/Finley/p573/solitons/KdVDeriv.pdf

[28] J. Harris, Ph.D. Dissertation, University of Maryland, (2005).

[29] User Manual of Nd:YAG Laser, Minitlite and PIV, Continuum.

[30] Hao Zhang, private communication, 2012.

[31] B. Beaudoin, Ph.D. Dissertation, University of Maryland, (2011).

[32] P. G. Drazin and R. S. Johnson, *Solitons: an introduction (2nd ed.)*, (Cambridge University Press, 1989).

[33] D.P. Grote, A. Friedman, I. Haber, S. Yu, Fusion Eng. Des 32-33, 193-200, (1996).

[34] Technical note, UMER-2012-0112-IH, BB, TPK

[35] Technical note, UMER-2012-0712-YM

[36] K. Tian, Ph.D. Dissertation, University of Maryland, (2008).

[37] H. Zhang, M.S. Thesis, University of Maryland, (2011).